Modeling of Solar Thermal Selective Surfaces and Thermoelectric Generators

by

Kenneth McEnaney

Submitted to the Department of Mechanical Engineering
in partial fulfillment of the requirements for the degree of

Master of Science in Mechanical Engineering

at the

MASSACHUSETTS INSTITUTE OF TECHNOLOGY

September 2010

Author .....
Department of Mechanical Engineering
August 8, 2010

Certified by .....
Gang Chen
Carl Richard Soderberg Professor of Power Engineering
Thesis Supervisor

Accepted by .....
David E. Hardt
Chairman, Department Committee on Graduate Theses

Modeling of Solar Thermal Selective Surfaces and Thermoelectric Generators

by

Kenneth McEnaney

Submitted to the Department of Mechanical Engineering
on August 8, 2010, in partial fulfillment of the
requirements for the degree of
Master of Science in Mechanical Engineering

Abstract

A thermoelectric generator is a solid-state device that converts a heat flux into electrical power via the Seebeck effect. When a thermoelectric generator is inserted between a solar-absorbing surface and a heat sink, a solar thermoelectric generator is created which converts sunlight into electrical power. This thesis describes the design and optimization of solar thermoelectric generators, with a focus on systems with high optical concentration which utilize multiple material systems to maximize efficiency over a large temperature difference. Both single-stage and cascaded (multi-stage) generators are considered, over an optical concentration range of 0.1 to 1000X. It is shown that for high-concentration Bi_2Te_3/skutterudite solar thermoelectric generators, conversion efficiencies of 13% are possible with current thermoelectric materials and selective surfaces. Better selective surfaces are needed to improve the efficiency of solar thermoelectric generators. In this thesis, ideal selective surfaces for solar thermoelectric generators are characterized. Non-ideal selective surfaces are also characterized, with emphasis on how the non-idealities affect the solar thermoelectric generator performance. Finally, the efficiency limit for solar thermoelectric generators with non-directional absorbers is presented.

Thesis Supervisor: Gang Chen
Title: Carl Richard Soderberg Professor of Power Engineering

Acknowledgments

This thesis would not have been possible without the help and support of many people. First I would like to thank my advisor, Gang Chen, for giving me the chance to work with him and the freedom to explore the topics covered in this thesis. I appreciate all his feedback regarding my work at MIT. I have also been extremely fortunate to work with a great team of lab members, especially Daniel Kraemer, who was always available to answer my questions and brainstorm and argue ideas; I couldn't have asked for better scientific collaborators and office mates. Leslie Regan, I appreciate your help and patience throughout the process.

I would also like to thank my mother, father, and sister for being a loving family, great people, and a lot of fun. In addition I'd like to thank Marc Marcussen, Al George, Charles Williamson, and Ray Erikson for their mentorship along my journey over the years. To all my family and friends I say thank you for keeping my spirits high through it all. Finally I would like to thank Jaime for her love and support throughout this long process. I could not have done it without her.

Contents

List of Figures

List of Tables

Chapter 1

Introduction

As a result of rising energy prices, concern for the environment, and a need for off-grid power systems, scientists and engineers have been working towards advancing our abilities to harvest the energy of the sun. Solar energy is abundant; the solar power striking the earth is nearly four orders of magnitude greater than the global power consumption: the world marketed energy consumption in 2007 was 495 quadrillion BTU, which is equivalent to a consumption rate of 16.5 terawatts[1], while the power of sunlight reaching the surface of the earth is approximately 90,000 terawatts. If all of the energy of the sun striking the surface of the earth could be captured with 100% efficiency, the annual world energy need could be satisfied in less than two hours. Although this is encouraging, the scale of solar power converters required to utilize this abundant yet diffuse resource is enormous. For example, if it was desired to capture the excellent solar resources of the desert southwest (averaging 6 kilowatt-hours per square meter per day[2]) in order to meet the annual US energy consumption (nearly 100 quadrillion BTU in 2007[3]), it would require the installation of 70,000 square kilometers of 20% efficient solar conversion devices. Assuming the conversion devices are installed such that they cover 50% of the available land, this solar farm would need to extend over 140,000 square kilometers - an area half the size of the state of Arizona.

Clearly there is a potentially huge demand for solar energy harvesting devices. The two major methods of harvesting solar energy for electricity are photovoltaics

and solar thermal heat engines. Photovoltaic technology dominates the solar electricity market, with 21 GW installed compared to only 0.6 GW for concentrating solar thermal power.[4] Solar photovoltaic growth has also rapidly outpaced the growth of concentrating solar thermal power: the amount of grid-connected solar photovoltaics has increased by a factor of 100 in the past ten years - a rate of increase of approximately 60% per year - while the quantity of installed concentrating solar thermal power has only increased 70% from 2005 to 2009.[4]

Despite the industry dominance of photovoltaics, solar thermal power has a large potential for growth. Especially attractive is its ability to store thermal energy and generate power when clouds pass or during the evenings. The first focus of this thesis is a technical challenge facing concentrating solar thermal energy: creating efficient selective surfaces. The second focus of this thesis is analyzing and designing efficient, scalable solar thermoelectric generators (STEGs).

1.1 Selective Surfaces

Solar thermal electricity plants, domestic hot water and process heat systems, solar heating and absorption chilling systems, and solar thermoelectric and thermionic generators all begin utilizing solar power by converting the sun's rays into heat. For these processes to be efficient, they must absorb as much of the sun's rays as possible while limiting the radiative heat loss from the absorbing surface. To do this, the solar absorbtance and infrared emittance of the absorbing surface must be optimized. Here the terms absorbtance and emittance are used to describe the properties of a surface, including the effects of surface structure, composition, and contamination; the National Institute of Standards and Technology recommends reserving the terms absorptivity and emissivity to describe intrinsic properties of a pure, perfectly smooth material[5]. To calculate the emittance of a surface, we begin with Planck's blackbody emission spectrum[6]:

$$E_b(T) = \int_0^\infty E_{b\nu}(T,\nu)\,d\nu = \int_0^\infty \frac{2\pi h\nu^3 n^2}{c_0^2\left[e^{h\nu/k_bT}-1\right]}d\nu \tag{1.1}$$

where E_b is the total blackbody emissive power, $E_{b\nu}$ is the spectral blackbody emissive power, $h = 6.626 \times 10^{-34}\,\mathrm{J\,s}$ is Planck's constant, ν is the radiation frequency, n is the index of refraction of the medium bounding the blackbody, $c_0 = 2.998 \times 10^{8}\,\mathrm{m\,s^{-1}}$ is the speed of light in a vacuum, and $k_b = 1.3807 \times 10^{-23}\,\mathrm{J\,K^{-1}}$ is Boltzmann's constant. The frequency can be related to the wavelength with the following equation:

$$\nu = \frac{c_0}{n\lambda} \tag{1.2}$$

For the calculations in this thesis, it is assumed that the medium bounding the surface is a vacuum, which has an index of refraction of 1. Since the index of refraction is constant, equation (1.1) can be rewritten in terms of the wavelength, λ:

$$E_{b\lambda}(T,\lambda) = \frac{2\pi h c_0^2}{n^2\lambda^5\left[e^{hc_0/n\lambda k_b T} - 1\right]} \tag{1.3}$$

Equation (1.3) describes the spectral emissive power of a blackbody, where $E_{b\lambda}$ is the energy flux in a given direction per unit time per unit surface area per unit frequency. The emissive power of a blackbody has a directional dependence also (direction is defined using polar coordinates, with θ as the polar angle and ϕ as the azimuthal angle). The spectral directional emissive power of a blackbody, $E'_{b\lambda}(T,\lambda,\theta,\phi)$, is defined as the energy flux in a given direction per unit time per unit wavelength per unit steradian per unit surface area (the prime symbol represents a directional property). At this point it is instructive to introduce the spectral radiative intensity of a blackbody, $I_{b\lambda}(T,\lambda)$. The spectral radiative intensity describes the energy flux per unit time per unit wavelength per unit steradian from a surface of unit area normal to the beam path. The difference between the spectral directional emissive power and the spectral directional radiative intensity is the reference area. For a blackbody, the spectral directional radiative intensity is actually independent of direction. The spectral directional emissive power is the spectral radiative intensity times the cosine of the polar angle:

$$E'_{b\lambda}(T,\lambda,\theta) = I_{b\lambda}(T,\lambda)\cos\theta \tag{1.4}$$

Integrating over the hemisphere capping a surface, the relationship between the emissive power and radiative intensity is derived, with the pi carrying units of steradians:

$$E_{b\lambda}(T,\lambda) = \pi I_{b\lambda}(T,\lambda) \tag{1.5}$$

Real surfaces do not emit as a blackbody, and their radiative intensity can be a function of direction. The spectral directional emittance, ϵ'_λ, is the fraction of the spectral blackbody radiative intensity emitted by a body in a given direction at a specific wavelength. In this thesis, it is assumed that the spectral directional properties of a material are independent of temperature. In reality this is not true due to temperature's effects on phonon and electron modes, but it allows for the calculation of an ideal surface without choosing a specific material system. The subscript e replaces b to denote the emitted radiative intensity of a real surface instead of a blackbody:

$$\epsilon'_\lambda(\lambda,\theta,\phi) = \frac{I'_{e\lambda}(T,\lambda,\theta,\phi)}{I_{b\lambda}(T,\lambda)} \tag{1.6}$$

The total hemispherical emittance of a surface, ϵ, is the ratio of the total emitted power to the power a blackbody would emit at the same temperature. Even with the assumption that the spectral directional emittance is not a function of temperature, the total hemispherical emittance is still a function of temperature due to the shift of the blackbody spectrum with temperature:

$$\epsilon(T) = \frac{\int_0^\infty \int_0^{\pi/2} \int_0^{2\pi} \epsilon'_\lambda(\lambda,\theta,\phi) I_{b\lambda}(T,\lambda) \cos\theta \sin\theta \, d\lambda \, d\theta \, d\phi}{\int_0^\infty \int_0^{\pi/2} \int_0^{2\pi} I_{b\lambda}(T,\lambda) \cos\theta \sin\theta \, d\lambda \, d\theta \, d\phi} \tag{1.7}$$

With this definition of emittance, the total emissive power can be calculated from the Stefan-Boltzmann Law, where $\sigma_{sb} = 5.670 \times 10^{-8}\,\mathrm{W\,m^{-2}\,K^{-4}}$ is the Stefan-Boltzmann constant:

$$E_e = \epsilon \sigma_{sb} T^4 \tag{1.8}$$

In addition to losses from a surface, the amount of energy absorbed by a surface must

also be calculated. The fraction of the incident (subscript i) spectral directional radiative intensity absorbed by a surface is the spectral directional absorbtance, α'_λ.

$$\alpha'_\lambda(\lambda,\theta,\phi) = \frac{[I'_{i\lambda}(\lambda,\theta,\phi)]_{absorbed}}{[I'_{i\lambda}(\lambda,\theta,\phi)]_{incident}} \tag{1.9}$$

To calculate the total power absorbed by a surface, the total hemispherical absorbtance of a surface, α, must be computed, where the absorbtance is the ratio of the total power absorbed to the total power incident on the surface. Kirchhoff's Law states that for any surface the spectral directional absorptance is equivalent to the spectral directional emittance: $\alpha'_\lambda = \epsilon'_\lambda$. Therefore the total hemispherical absorptance of a surface, α, under an incident spectral directional radiative intensity $I'_{i\lambda}$, can be defined as:

$$\alpha = \frac{\int_0^\infty \int_0^{\pi/2} \int_0^{2\pi} \epsilon'_\lambda(\lambda,\theta,\phi) I'_{i\lambda}(\lambda,\theta,\phi) \cos\theta \sin\theta \, d\lambda \, d\theta \, d\phi}{\int_0^\infty \int_0^{\pi/2} \int_0^{2\pi} I'_{i\lambda}(\lambda,\theta,\phi) \cos\theta \sin\theta \, d\lambda \, d\theta \, d\phi} \tag{1.10}$$

It is convenient to write the denominator of equation (1.10) as the total hemispherical incident irradiance H:

$$H = \int_0^\infty \int_0^{\pi/2} \int_0^{2\pi} I'_{i\lambda}(\lambda,\theta,\phi) \cos\theta \sin\theta \, d\lambda \, d\theta \, d\phi \tag{1.11}$$

Comparing equations (1.10) and (1.7), it is clear that the total hemispherical absorptance is equal to the total hemispherical emittance if the incident spectral directional radiative intensity is equal to the blackbody spectral directional radiative intensity at the temperature of the surface. For solar selective surfaces, these two spectra have little overlap: the solar spectrum falls mainly between 300 nm and 2.5 µm, while the blackbody spectrum at a temperature below 700 K is almost exclusively at wavelengths 2 µm and longer, as seen in figure 2-3 (the solar spectrum on earth is discussed in detail in section 2.2). To create effective solar thermal devices, scientists and engineers have found or developed selective surfaces that show wavelength-dependent properties such that they have high absorbtance in the solar spectrum and low emittance in the infrared spectrum.

1.1.1 Concentrating Solar Devices

In this thesis, the performance of selective surfaces with both non-concentrating and concentrating optics are calculated. Optical concentrating devices are described by their optical concentration ratio, C_{opt}, which is the ratio of the area of the input beam to the area of the output beam[7]. The collector flux (the intensity of light incident on the collector) is the optical concentration ratio times the incident solar flux times the optical efficiency:

$$H_{surf} = C_{opt} H_{sol} \eta_{opt} \tag{1.12}$$

The main optics architectures for solar thermal devices are non-concentrating flat-panel devices, low-concentration devices, adjustable concentrators, single-axis tracking systems, and dual-axis tracking systems.[8] The typical geometry of a flat-plate collector is either a flat absorbing surface under insulated panes of glass, or a set of evacuated glass tubes with an absorbing surface inside. These non-concentrating solar absorbers ($C_{opt} = 1$) can see a solar flux less than $1\,\mathrm{kW\,m^{-2}}$ due to non-ideal angles of incidence and other atmospheric effects such as clouds; they can also see a solar flux greater than this value if the air mass is less than 1.5, if the panel is oriented normal to the sun, or if any of the local atmospheric particle concentrations are less than those specified in ASTM G 173-03. Low-concentration solar thermal devices do not require tracking, yet can have a C_{opt} up to 2 by using non-imaging optics with wide acceptance angles, such as light cones, compound parabolic collectors (CPCs), or strip (Fresnel) concentrators[9]. If the acceptance angle of the optics is decreased, these devices require seasonal, weekly, or even daily adjustment. With an acceptance angle of 6°, daily adjustment is required but the optical concentration ratio can reach $C_{opt} = 10$.[10] The most common type of single-axis concentrating solar thermal system is the solar trough[11], which harnesses solar energy for use with turbines to generate electricity. These systems can reach an optical concentration ratio of $C_{opt} = 100$.[8] Two other single-axis tracking systems are Fresnel concentrators[12] and Fresnel reflectors[13]. There are two main architectures for dual-axis tracking

systems: dish concentrators and solar tower systems. Dish concentrators frequently use Stirling engines at their focal point, reaching an optical concentration ratio of $C_{opt} = 750$.[14] Solar towers, also known as central receivers, employ many small mirrors (heliostats) focusing light on one central absorbing surface and can create optical concentration ratios of $C_{opt} = 1,000$ or more.[15]

Table 1.1: Operating points of common solar-energy harvesting devices[8,10,11,14,15].

System	C_{opt}	Operating Temperature [°C]
Flat panel	0.5 - 2	100 - 300
Adjustable	2 - 10	100 - 300
Trough	15 - 100	100 - 400
Dish/Tower	500 - 1000+	500 - 1200+

1.2 Thermoelectrics

One possible method of converting the sun's heat to electricity is via a thermoelectric generator (TEG). A thermoelectric generator is a device that converts a heat flux into electrical power. Thermoelectric devices have been used in various applications from sensing to cooling to power generation. Most of the power generation research has been geared toward space missions and waste heat recovery. However, we hope to show that a good solar thermoelectric generator design could compete with other terrestrial solar technologies.

1.2.1 The Thermoelectric Effects

As their name suggests, thermoelectric effects are interactions between heat and electricity. The first report of a thermoelectric effect was in 1821, by the German-Estonian scientist Thomas Johann Seebeck. When two ends of a material are at different temperatures, a voltage difference develops between the ends of the material. This effect is called the Seebeck effect, and the constant of proportionality between the temperature difference and the voltage difference is the Seebeck coefficient, S (Eq. (1.13)).

The symbol α is commonly used for the Seebeck coefficient, however in this thesis α will be used for absorbtance of surfaces.

$$S = -\frac{\Delta V}{\Delta T} \tag{1.13}$$

The second observed thermoelectric effect was the Peltier effect, named after the Frenchman Jean Charles Peltier. Peltier noticed that when a current passed through a juction of dissimilar metals, the junction could be cooled. The cooling heat flux absorbed at the junction, Q_p, is proportional to the current, I, with the constant of proportionality the Peltier coefficient, Π_{ab}, where in the notation of Goldsmid[16] the subscript ab denotes that this effect occurs at the junction between two materials, a and b.

$$Q_p = \Pi_{ab} I = (\Pi_b - \Pi_a)\, I \tag{1.14}$$

In 1854, William Thomson (Lord Kelvin) derived a relationship between the Seebeck effect and the Peltier effect. In doing so, he discovered a third thermoelectric effect, the Thomson effect, where the passage of current through a material with a temperature gradient causes the absorption of a reversible heat per unit volume, q_t, proportional to the current density $J = I/A$ and the temperature gradient (Eq. (1.15)). The Thomson coefficient is sometimes denoted by the variable μ, but in this thesis Goldsmid's convention of representing the Thomson coefficient with γ will be will be used in order to prevent confusion with the electrochemical potential.

$$q_t = \gamma J \frac{dT}{dx} \tag{1.15}$$

The Kelvin relationships between the Seebeck, Peltier, and Thomson coefficients are described in equations (1.16) and (1.17).

$$\Pi = TS \tag{1.16}$$

$$\gamma = T\frac{\partial S}{\partial T} \tag{1.17}$$

1.2.2 Thermoelectric Device Performance

Thermoelectric materials can be used as refrigerators or as power conversion devices. In refrigeration mode, current running through the thermoelectric device absorbs heat at the cold junction and releases it at the hot end of the junction. In power generation mode, a temperature gradient causes a Seebeck voltage, which drives a current around a circuit. By applying an energy balance on the thermoelectric material the ideal coefficient of performance of a thermoelectric refrigerator, ϕ_{max}, or the ideal efficiency of a thermoelectric generator, η_{max}, can be calculated as a function of the thermoelectric material properties and the temperatures[16]:

$$\phi_{max} = \left(\frac{T_c}{T_h - T_c}\right)\left(\frac{\sqrt{1 + Z\overline{T}} - T_h/T_c}{\sqrt{1 + Z\overline{T}} + 1}\right) \tag{1.18}$$

$$\eta_{max} = \left(\frac{T_h - T_c}{T_h}\right)\left(\frac{\sqrt{1 + Z\overline{T}} - 1}{\sqrt{1 + Z\overline{T}} + T_h/T_c}\right) \tag{1.19}$$

where T_c is the cold-side temperature, T_h is the hot-side temperature, and $\overline{T}$ is the arithmetic mean temperature (all measured in absolute temperature). For a thermoelectric material, the product ZT is called the dimensionless figure of merit, which can be defined as[17]:

$$ZT = \frac{S^2\sigma}{\kappa}T \tag{1.20}$$

where σ is the electrical conductivity and κ is the thermal conductivity of the material. In equation (1.19), the first ratio is the Carnot efficiency. The second ratio is clearly less than unity, so a thermoelectric generator can be thought of as a heat engine whose performance is limited by the Carnot efficiency. The higher the dimensionless figure of merit, the closer the thermoelectric generator comes to the ideal Carnot engine. It is important to note that equations (1.18) and (1.19) were derived assuming

that the materials' properties do not change as a function of temperature. In fact, the material properties have a strong dependence on temperature, so that as the temperature increases the ZT of a material will rise to a peak value and then decrease as the temperature exceeds the optimum temperature. This strong temperature-dependence means there is not just one best thermoelectric material; it is crucial to know the temperature range of the application in order to choose which thermoelectric material to use. When considering temperature-dependent properties, the term $Z\overline{T}$ in equations (1.18) and (1.19) should be replaced by a mean dimensionless figure of merit, $\overline{ZT}$. Unfortunately there is no easy way to calculate a mean dimensionless figure of merit besides solving Domenicali's equations to calculate the efficiency (described in chapter 3) and then backing out the effective $\overline{ZT}$ using equations (1.18) and (1.19).

1.2.3 Thermoelectric Materials

From the time of Seebeck's discovery in 1821 until the beginning of the twentieth century, thermoelectricity was used almost exclusively as a detector, either to measure temperature via a thermocouple or to measure radiant energy with a thermopile[18]. Lenz had demonstrated in 1838 that the Peltier effect could be used to freeze ice, yet this application of thermoelectricity was not pursued until the early twentieth century because the dimensionless figure of merit of the best-known thermoelectric materials was very low.[19] In the early twentieth century, scientists discovered the high dimensionless figure of merit of certain semiconductors, in particular bismuth telluride, bismuth antimonide, and zinc antimonide[20]. These materials, with ZTs approaching 1, opened up the potential of using thermoelectrics for cooling and power generation at temperatures up to 420 °C[20]. For most of the second half of the twentieth century, no major improvements in the dimensionless figure of merit were made, although materials with a dimensionless figure of merit approaching one were reported in higher temperature ranges, including lead telluride[21, 22] and silicon germanium alloys[23,24]. The apparent limit of ZT = 1 remained unbroken until 1993, when Hicks and Dresselhaus suggested that low-dimensional structures such as one-dimensional conductors[25] and quantum-well structures[26] could have a high dimensionless fig-

ure of merit. These papers generated a wave of interest in thermoelectrics, and in the past two decades materials have been created with dimensionless figures of merit over 1.5[27–29]. Bulk thermoelectric materials including SiGe alloys, skutterudites, and various tellurium compounds (PbTe, Bi_2Te_3, Sb_2Te_3, and others) all have dimensionless figures of merit near or above unity over a variety of different temperature ranges.[30] Many of these materials use nanostructures to achieve their high dimensionless figure of merit.[31]

The solar thermoelectric generators in this thesis operate in the low- to mid-temperature range (up to approximately 600 °C). This is done because the upper limit for the skutterudites from our collaborators have an upper limit of 600 °C. If this temperature was exceeded, a high-temperature third stage (most likely made of silicon-germanium) would have to be added to the system, adding additional complications to the system. A three-stage system may be considered in the future. The properties of the thermoelectric materials used in this thesis are presented in appendix A. The doped Bi_2Te_3 compounds used here have an upper temperature limit of 250 °C; the skutterudites have an upper temperature limit of 600 °C. These materials are provided by collaborators under the supervision of Professor Zhifeng Ren at Boston College.

1.3 Thesis Outline

Chapter 2 of this thesis will investigate the properties of selective surfaces for solar thermal systems. It begins with a review of selective surface optimization, followed by a description of the solar spectrum. Ideal selective surfaces are then defined such that the performance of solar thermal systems with these selective surfaces is optimized. Non-ideal selective surfaces are considered next, which leads to an analysis of how non-ideal selective surfaces should be optimized. Chapter 2 ends with a look at the state of the art in selective surface technologies. Chapter 3 focuses on the design and optimization of a concentrating solar thermoelectric generator. First a method for optimizing both single-material and multi-material (cascaded and segmented) ther-

moelectric generators is presented. These thermoelectric generators are incorporated into solar thermoelectric generators, and the optimization and predicted efficiency of these devices is presented. Chapter 3 concludes with a look at future modeling efforts for solar thermoelectric generators. Chapter 4 combines the selective surface and thermoelectric models to predict the maximum efficiency of a STEG. The thesis closes with a summary of the work done, and a proposed avenue for continuing research in this field.

Chapter 2

Selective Surfaces

This chapter analyzes the performance of a selective surface. First, a history of selective surfaces is presented. Next, an explanation of the solar spectrum is followed by the introduction of the transition wavelength and the method of optimizing it for solar heat engines. This analysis is then performed for concentrating solar heat engines, and then is extended to non-ideal selective surfaces. The discussion of non-ideal selective surfaces leads to calculations on how to best improve existing selective surface materials. It is important to note that this thesis merely characterizes selective absorbers; there is no attempt to describe how these materials would actually be manufactured (see section 2.9 for a summary of existing selective surface materials). The calculations in this chapter assume that the surface has an emittance that is a function of wavelength *but not a function of direction.* Leveraging direction-dependent emittance to create better selective surfaces is discussed in section 5.2.

2.1 History of Selective Surfaces

Very early in man's attempt to harvest the sun's energy, it was discovered that black surfaces absorbed the most heat. In the first era of solar energy harvesting experiments, dating from the early 1600s through the early twentieth century, scientists and inventors utilized black surfaces for solar absorbers. While no discussion is given to the selectivity of the black surface, some experimenters realized that glass plates

allow solar radiation to pass, while trapping heat from a hot surface.[32] Simonin described this effect in 1876:

> The boiler is of copper, which of all the common metals is the best conductor of heat; it is blackened on the outside, because black possesses the property of absorbing all the heat rays, just as white reflects them; and it is inclosed in a glass envelope, glass being the most diathermanous of all bodies; that is to say, the most permeable by the rays of luminous heat. Glass further possesses the property of resisting the exit of these same rays after they have been transformed into dark rays on the blackened surface of the boiler.[33]

In his 1915 review of solar energy utilization, Ackermann notes that "the diathermicity of each substance varies with the nature of the source of heat."[32] Clearly it was well-understood that the transmittance of a material was dependent on the temperature of the source of radiation. We can assume the author knew that this was the result of the wavelength distribution of different sources of heat, as the work of Planck[6] had been published 14 years prior, and Wien's displacement law had been known for nearly a quarter-century[34]. In the following years, researchers studied the use of glass sheets to add resistance to the radiative and convective paths as a way to decrease surface losses. At the International Conference on the Use of Solar Energy in 1955, Tabor introduced the idea of using a selective surface as a solar absorber.[35] The selective surface would have wavelength-dependent properties such that it would absorb strongly in the solar spectrum while emitting very little in the infrared. This would allow the solar plant engineer to design systems without concentration that could operate at higher temperatures. Tabor calculates that the amount of solar radiation at wavelengths greater than 2 µm is negligible, and the amount of emission at wavelengths shorter than 2 µm is less than 0.2% for a 600K blackbody. From this basic analysis, the ideal "transition wavelength" of 2 µm was established:

> From this it follows that if surfaces can be prepared so that they differentiate in their absorption, reflection or transmission characteristics

> between wavelengths above 2 microns and wavelengths below 2 microns, it may be possible to change the emittance, which is a property for wavelengths above 2 microns, without affecting the solar energy transmission or absorption coefficients, which are properties for wavelengths below 2 microns.[35]

Tabor continues with his declaration that the transition wavelength should occur between 2-3 microns:

> Thus it follows that, if on the one hand a metal has low absorption for long wavelengths but on the other can be made to appear black, i.e. to have high absorption in the visitble spectrum, then there must be some part of the spectrum where transition occurs. If this transition is reasonably sharp and occurs at between 2-3 microns, the required reflection-absorption high pass filter is obtained.[35]

This work by Tabor references works by many people who were studying wavelength-dependent transmittance of materials[36,37]. Tabor deserves credit for being the first to propose the idea of a selective absorber for solar thermal systems. He describes one such system, and its daily and yearly power outputs, in a 1956 paper[38].

Since Tabor's original conference paper, many authors have investigated the ideal transition wavelength for a selective surface as a function of temperature and concentration, including Shaffer[39], Gillette[40], Edwards *et al.*[41], Liebert and Hibbard[42], Cross[43], Schmidt[44], Jurisson *et al.*[45], Spitz[46], Pasquetti and Papini[47], Seraphin[48], and Mills[49]. However, all of these authors approximate the solar spectrum as a blackbody at a temperature in the range of 5700 to 6000 K. Most likely this was done to ease the computation, as a more realistic (i.e. complicated) solar spectrum at the earth's surface was presented as early as 1940 by Moon[50]. Moon's work was known by many of the above authors, and is even cited by Shaffer and Edwards *et al.*. Mills rationalizes ignoring the atmospheric absorption bands: "To incorporate particular absorption bands would require that K [the absorption] be a strong function of wavelength. However, in the following we take K to be con-

stant, which introduces a small spectrally induced error in P_N. As we will later show, this error is quite small." While it is true that the maximum efficiency is not affected much by ignoring atmospheric absorption bands, the ideal transition wavelength of an ideal absorber is strongly affected by these bands. This is one of the most important conclusions of this thesis, and it is described in detail in the following sections.

2.2 The Solar Spectrum

Almost all published ideal selective surface calculations were made before the 1970s, when a lack of computational power led researchers to model the solar spectrum as a blackbody emitter at approximately 5800 K. As will be shown in this chapter, the results obtained when using a standardized solar spectrum (such as AM1.5) produce dramatically different optimal selective surface properties than can be obtained if one treats the solar spectrum as that of a blackbody.

The first proposed standard curves for the amount of solar radiation reaching the earth's surface were published by Moon in 1940[50]. In this paper, Moon gives an extensive review of all the solar constant and atmospheric absorption measurements made prior. Moon then gives the result of his calculated spectra as a function of the mass of air through which the solar radiation travels. Moon's curves were ultimately replaced by the calculations of Bird *et al.*[51], which became the 1982 ASTM standards E-891-82 and E-892-82. These two standards were updated several times and finally combined into one standard, ASTM G159-98. The spectra were recalculated in 1999 to extend deeper into the ultraviolet, to homogenize the wavelength step size, and to modify the simulated atmospheric conditions. The resulting standard is ASTM G 173-03[52], which gives two different spectra. Both of these spectra describe the amount of light reaching a surface after is has passed through an "air mass 1.5," which is a column of air 1.5 times more massive than a column of air normal to the earth's surface. The solar zenith at which this occurs is approximately $\theta = \arccos(1/1.5)$. The angle is not exactly just the inverse cosine of 1/1.5 because the model takes into account the curvature of the atmosphere and the density profile of the atmosphere.

The two spectra in ASTM G 173-03 differ in the acceptance angle and the orientation of the reference surface. One spectrum, Air Mass 1.5 Direct Normal Spectral Irradiance, sometimes called "AM1.5 Direct + Circumsolar" or simply "AM1.5," is the calculated solar radiation incident on a surface normal to the sun through a 5.8° field of view (2.9° half-angle, 8.05×10^{-3} steradians). For Air Mass 1.5 Global Total Spectral Irradiance on a 37° sun-facing tilted surface, or "AM1.5G," the surface is tilted 37° in the direction of the sun, but since an air mass of 1.5 requires a zenith angle of 48.236°, there is an angle of incidence of 11.236°. The calculations in this standard are based on the measured solar radiation outside the atmosphere, AM0, which can be found in the the ASTM standard ASTM E 490-00a[53]. All three of these spectra are plotted in figure 2-1. The heat flux density integrated over all wavelengths for AM0 is the solar constant, $1366.1\,\mathrm{W\,m^{-2}}$. The heat flux density of AM1.5 Direct + Circumsolar is $900.1\,\mathrm{W\,m^{-2}}$, which is smaller than the AM1.5G value of $1000.4\,\mathrm{W\,m^{-2}}$ because the AM1.5G spectrum incorporates the diffuse (global) light. However, diffuse light cannot be concentrated, so in this thesis AM1.5 Direct + Circumsolar is used as the solar spectrum unless otherwise noted.

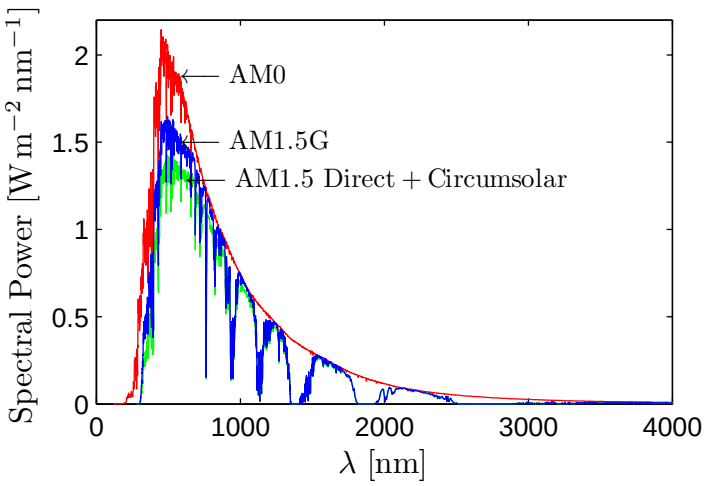

Figure 2-1: Solar spectra as defined by ASTM E 490-00a and ASTM G 173-03.

2.3 Surface Efficiency

The performance of a selective surface at a temperature T_h can be quantified by the surface efficiency, η_{surf}, which is the ratio of the net heat captured by the selective surface, $Q_{net} = q_{net}A_{surf}$, to the total hemispherical irradiance incident on the surface, $H_{surf}A_{surf}$. The area of the surface cancels out of both terms, and the analysis can be done in terms of heat fluxes:

$$H_{surf} = \int_0^\infty H_{\lambda,surf} d\lambda \tag{2.1}$$

$$\eta_{surf} = \frac{q_{net}}{H_{surf}} \tag{2.2}$$

Here the net heat is the absorbed solar flux minus the emitted radiation. Also included in the net heat is the incident long-wavelength radiation from the environment at a temperature T_{amb}:

$$q_{net}\left(\epsilon_\lambda, T_h\right) = \int_0^\infty \epsilon_\lambda \left[H_{\lambda,surf}\left(\lambda\right) - E_{b\lambda}\left(T_h, \lambda\right) + E_{b\lambda}\left(T_{amb}, \lambda\right)\right] d\lambda \tag{2.3}$$

The denominator of equation (2.2), H_{surf}, does not include the long-wavelength environmental radiation. This is merely by convention: the photovoltaics industry ignores the long-wavelength radiation when calculating efficiency, as the long-wavelength radiation is usually at photon energies much less than the bandgap of the material. Thus the long-wavelength radiation is not counted as a gain to the system, but as an effect that reduces the losses of the system.

As discussed in the preceding literature review, for an ideal absorber the wavelength-dependent emittance should be either 1 when the incident intensity at a given wavelength is larger than the blackbody intensity at that wavelength, or zero when the converse is true. The most basic implementation of this idea is an emittance profile that is a step function, transitioning from $\epsilon_\lambda = 1$ to $\epsilon_\lambda = 0$ at a transition wavelength, λ_t. The plot of the emittance spectrum of an ideal selective surface superimposed over the solar spectrum and the spectrum of a 400 K blackbody is presented in fig-

ure 2-2. As we can see from this figure, the solar spectrum and the low-temperature blackbody curve have no significant overlap: both are virtually zero from 2500 nm to 4000 nm. Thus the transition from high absorptance to low emittance should occur over this nearly empty region. For the ideal selective surface shown in figure 2-2, the optimal transition wavelength is 2510 nm, which is where the tabulated AM1.5 spectrum drops to nearly zero (less than $1 \times 10^{-3}\,\mathrm{W\,m^{-2}\,nm^{-1}}$). An ideal selective surface with this transition wavelength has a total hemispherical absorptance of 1 and a total hemispherical emittance of 1.5×10^{-4}, leading to a surface efficiency over 99.9%.

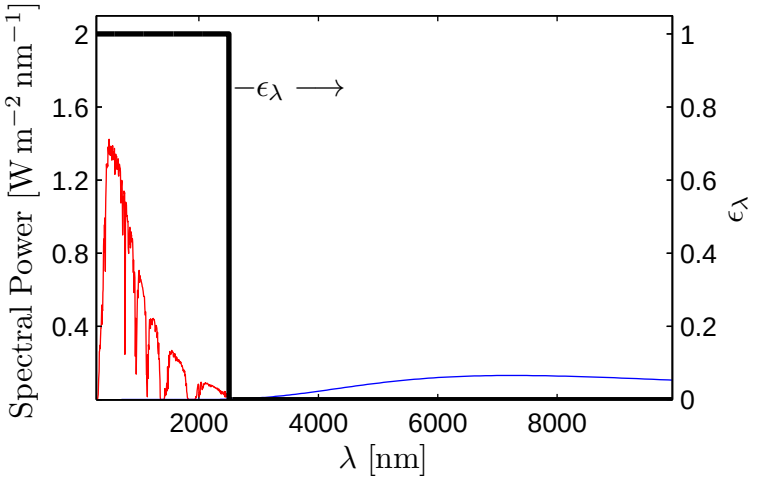

Figure 2-2: AM1.5 solar spectrum (red) and radiative spectrum of a 400 K blackbody (blue), with superimposed optimal emittance profile (black).

The selective surface design problem becomes interesting because as the temperature of the radiating blackbody increases, its spectrum grows in magnitude and shifts to shorter wavelengths (Fig. 2-3). Results for the optimal transition wavelength as a function of surface temperature are given in figure 2-4. These transition wavelengths are calculated by computing the blackbody radiation curve at each temperature (Eq. (1.3)), and then finding the transition wavelength that maximizes the net heat flux (Eq. (2.3)).

In figure 2-4, there are abrupt jumps in the optimal transition wavelength curve. An explanation of these sharp transitions is in order. As the surface temperature

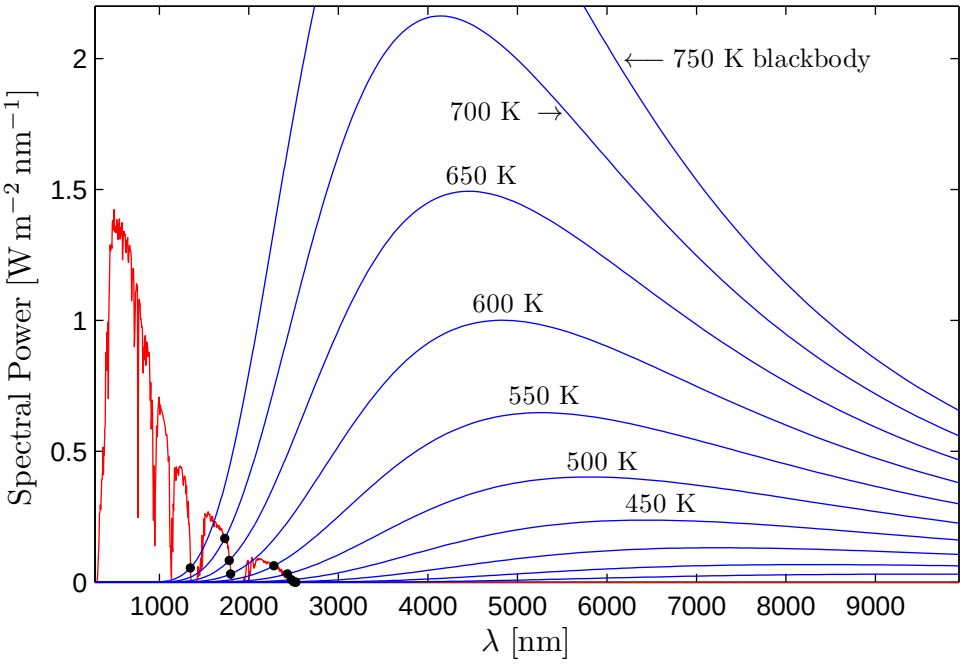

Figure 2-3: Multiple blackbody spectra plotted against AM1.5 spectrum.

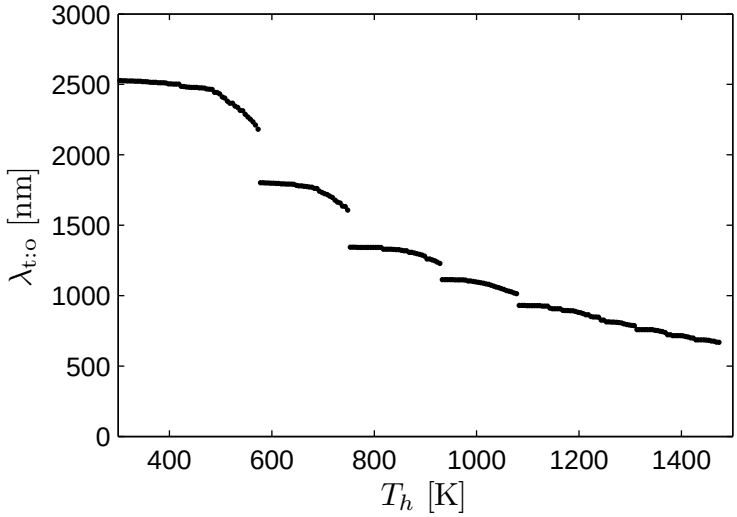

Figure 2-4: Optimal selective surface (step emittance) transition wavelength $\lambda_{t:o}$ as a function of temperature. Step size between dots is 5 K.

increases, the blackbody curve grows and shifts to the left (see figure 2-3). Many blackbody curves intercept a falling edge of AM1.5, as seen by curves for T_h = 600, 650, and 700 K crossing the solar spectrum in the range of 1750 - 1800 nm. When the temperature gets hot enough that it "spills over" one of these falling edges (e.g. when $T_h = 750\,\mathrm{K}$), it will cross the solar spectrum in three places: two through the relatively flat-topped hump to the left of the 1750-nm falling edge, and once more at the shorter-wavelength falling edge at 1345 nm. Although a transition wavelength at the right-most intercept of 1610 nm will absorb more solar intensity, it will also cause more energy to be radiated from the surface. The net effect is that the integral between the curves from 1345 nm to 1610 nm represents a net loss of energy, so the optimal transition wavelength will occur at the falling edge of 1345 nm.

The surface efficiency is plotted in figure 2-5 as a function of λ_t and surface temperature. We can see that the selective surface efficiency goes to 1 as the surface temperature goes to room temperature because as the surface temperature decreases, the overlap between the solar spectrum and the surface radiative spectrum goes to zero. When this happens, the ideal selective surface will be able to fully absorb the solar spectrum ($\alpha \approx 1$) while reducing the emitted radation to zero ($\epsilon \approx 0$).

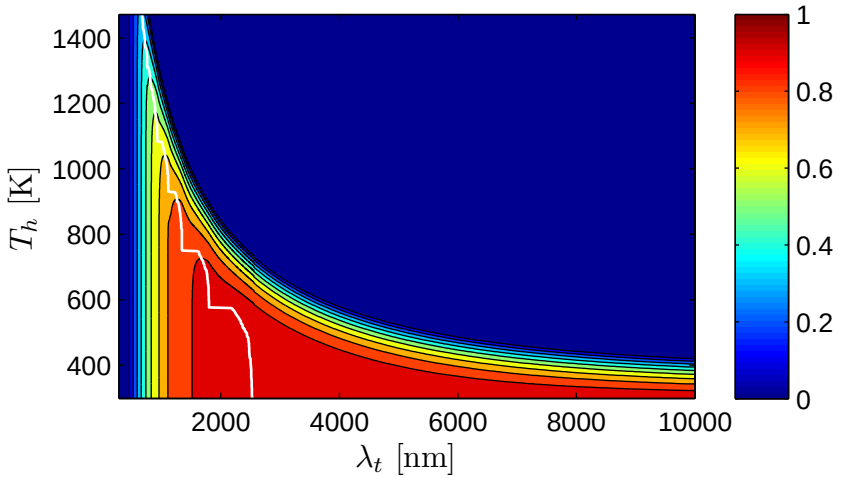

Figure 2-5: Selective surface efficiency η_{surf} as a function of transition wavelength λ_t and operating temperature T_h. The optimal λ_t as a function of T_h is superimposed in white.

The ideal emittance profile is a step function from 1 to 0, but it is important to optimize the performance of more realistic surfaces. A simple model of a spectral emittance profile is shown in figure 2-6, where a is the short-wavelength emittance, e is the long-wavelength emittance, λ_t is the transition wavelength, and w is the width of the transition. In addition to considering the ideal emittance profile, this thesis will analyze emittance profiles that deviate from $a = 1$, $e = 0$, and $w = 0$.

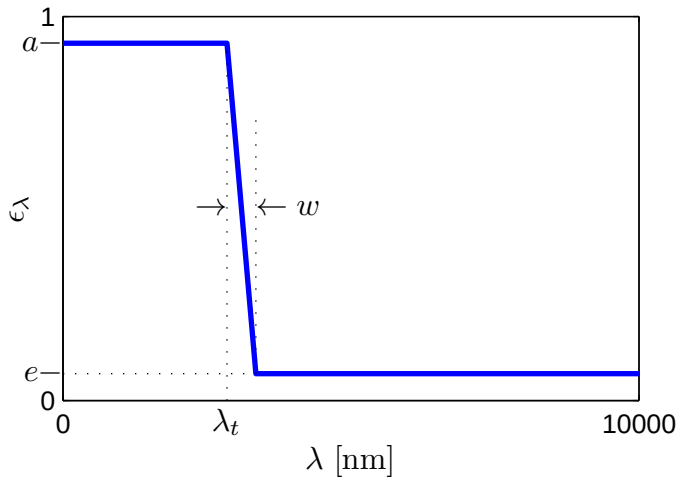

Figure 2-6: Model of a simplified emittance profile, where a is the short-wavelength emittance, e is the long-wavelength emittance, λ_t is the transition wavelength, and w is the width of the transition.

2.4 Optimizing a Solar Carnot System

The previous section determined the optimal transition wavelength to maximize the net radiative heat absorbed by the selective surface. As a result, the analysis implied that the best solar harvesting happens at low temperatures. However, the efficiencies of many systems are not just a funcion of the net heat flux, but also of the temperature difference across the cycle. In this subsection, the optimal selective surface for a system comprising a selective surface and a Carnot cycle is characterized. This is an appropriate choice since selective surfaces are commonly found at the high-temperature side of a working fluid cycle. The Carnot cycle operates at the efficiency

limit defined by the second law of thermodynamics. The cycle will have a variable hot-side temperature, T_h, and a constant cold-side temperature, $T_c = 20\,^{\circ}\mathrm{C}$. It is assumed there is no optical concentration on the collector. The goal of the optimization will be to maximize the efficiency of the entire selective surface/Carnot cycle system.

The efficiency of a Carnot cycle, η_c, is defined as:

$$\eta_c = 1 - \frac{T_c}{T_h} \tag{2.4}$$

As we can see from Eq. (2.4), increasing the hot-side temperature increases the Carnot efficiency. However, increasing the hot-side temperature also increases the radiative losses at the selective surface, and it also increases the overlap between the solar spectrum and the radiated spectum, making it harder to design an effective selective surface. Combining the surface efficiency and the cycle efficiency, we can calculate the total efficiency of the system, η_{sys}, from Eq. (2.5).

$$\eta_{sys} = \eta_{surf}\eta_c \tag{2.5}$$

The efficiency of the ideal system is a function of T_c, T_h, H_{surf}, and the shape of the spectral emittance profile. Figure 2-7 shows the system efficiency for H_{surf}=AM1.5 as a function of λ_t and T_h for the case where $a = 1$, $e = 0$, and $w = 0$. The maximum system efficiency of 55% occurs at a temperature of 838 K with a transition wavelength of 1327 nm. In real systems, it is improbable that $a = 1$ and $e = 0$; the maximum system efficiency as a function of a and e is plotted in figure 2-8. This figure shows that for selective surfaces connected to Carnot cycles under no optical concentration, minimizing the emitted radiation is more important than maximizing the absorbed radiation. This is because maximum system efficiencies occur at high temperatures due to the temperature dependency of the Carnot cycle, and surfaces over 355 K have the potential to emit more power than they can absorb through the solar spectrum ($E_b(355\ \mathrm{K}) = 900.5\,\mathrm{W\,m^{-2}}$ compared to $H_{AM1.5} = 900.1\,\mathrm{W\,m^{-2}}$). Despite the clear incentive to prioritize the long-wavelength emittance over the short-wavelength absorptance, many materials today have excellent absorptances but still

have high emittances.[54]

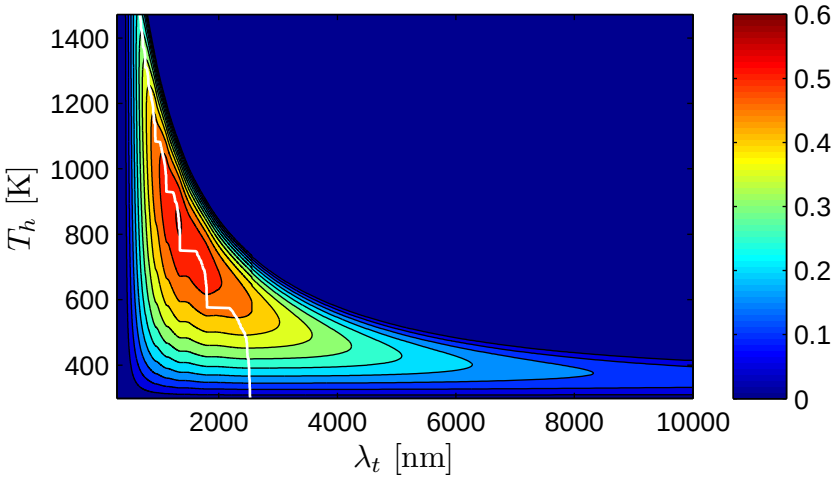

Figure 2-7: System efficiency η_{sys} as a function of transition wavelength λ_t and operating temperature T_h. The optimal λ_t as a function of temperature is superimposed in white.

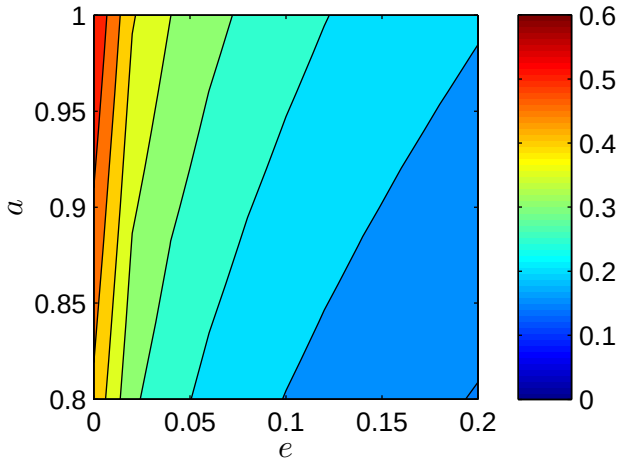

Figure 2-8: Maximum system efficiency η_{sys} as a function of short-wavelength emittance a and long-wavelength emittance e.

2.5 Optical Concentration

Optical concentration is almost always used in large-scale solar thermal systems such as solar towers and solar troughs, but an optical concentration ratio of greater than 3

is rarely used on small systems such as rooftop hot water installations. Concentration has a major effect on the efficiency of a system. First, the intensity of the incident spectrum increases, providing more power per unit area of device. This allows the incident flux to dominate the emittance losses, so higher-temperature operation can be achieved without the surface efficiency penalty it carries at low concentrations. In addition, with optical concentration the intersection of the solar spectrum and the emitted spectrum moves to longer wavelengths for a given temperature (Fig. 2-9). This causes more of the solar spectrum to stay to the left (the absorbing side) of the transition wavelength. Thus the optical concentration of a solar power system drives the requirements for the selective surface. In this chapter of the thesis it is assumed that the optical efficiency of the concentrating system is 1, so that all the light that entering the aperture of the concentrator irradiates the selective surface.

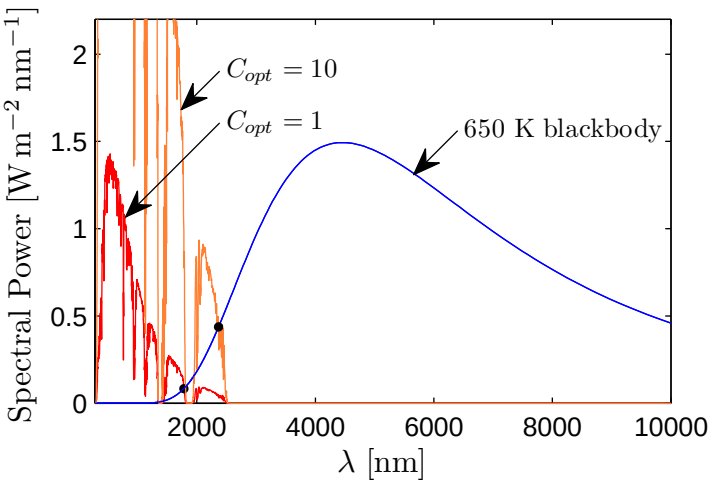

Figure 2-9: The AM1.5 solar spectra with $C_{opt} = 1$ and $C_{opt} = 10$ plotted with a 650 K blackbody.

Assuming there is an ideal selective surface, the overall system efficiency as a function of the optical concentration and temperature is seen in figure 2-10. The optimal transition wavelength as a function of optical concentration and hot-side temperature is shown in figure 2-11. This transition wavelength map has three broad plateaus: one between 1300 and 1350 nm, one between 1750 and 1800 nm, and one plateau above 2450 nm. Absorption of solar energy by atmospheric water vapor creates sharp

notches in the solar spectrum; these absoprtion bands are what cause the lower two broad plateaus in the transition wavelength map. The plateau above 2450 nm is due to the fact that very little solar radiation leaves the sun at wavelengths longer than 2450 nm, and absorption by water vapor in the Earth's atmosphere further diminishes the intensity in this regime. Therefore a transition wavelength beyond approximately 2500 nm does not increase absorption and only results in increased emission losses. In figure 2-10, the maximum efficiency for a given concentration is superimposed in black. When this same maximum efficiency curve is superimposed on the map of ideal transition wavelengths (figure 2-11), it can be seen that these maxima lie in the plateaus of approximately 1350, 1750, and 2500 nm. For each optical concentration there is a transition wavelength and temperature that maximizes the system efficiency; these values are plotted in figure 2-12.

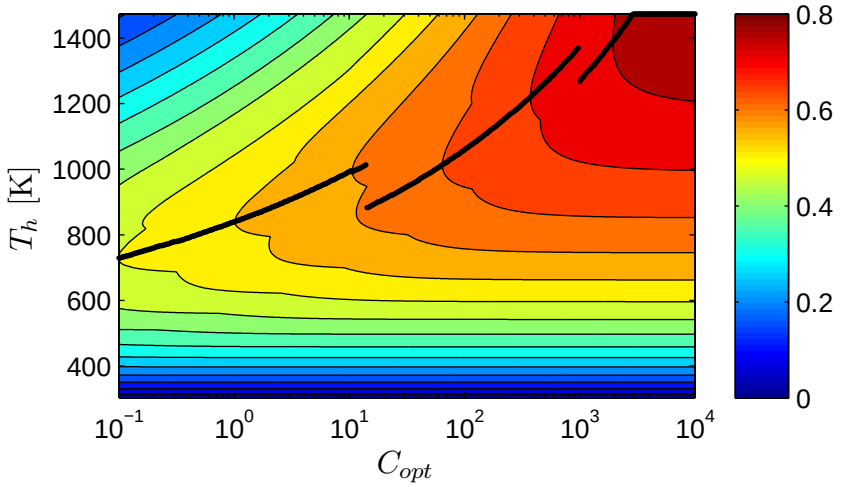

Figure 2-10: Maximum system efficiency as a function of hot-side temperature and optical concentration. The optimal temperature for a given C_{opt} is traced in black.

An explanation is in order for why these discrete jumps occur. It is important to notice that the jumps only occur in temperature and transition wavelength, not in efficiency. Essentially, there are two competing efficiency curves: one at the shorter transition wavelength with higher temperatures, and one at the longer transition wavelength with lower temperatures. At the concentration where these two operational curves cross, there is a corresponding jump in transition wavelength and in

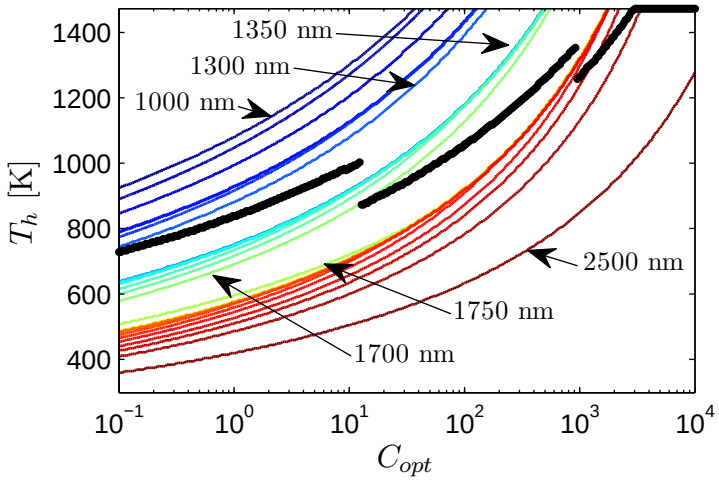

Figure 2-11: Optimal transition wavelength as a function of hot-side temperature and optical concentration. Contour intervals are 50 nm. The maximum point for a given C_{opt} is traced in black.

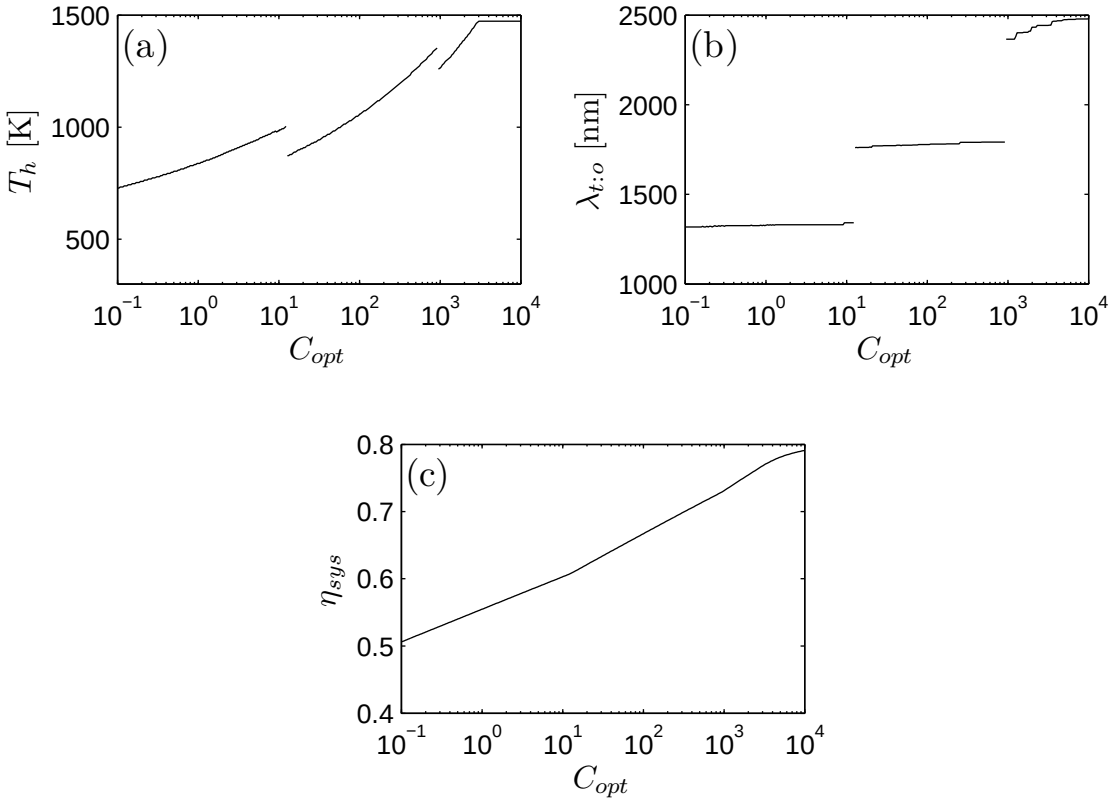

Figure 2-12: For a given concentration, there is (a) an operating temperature and (b) a transition wavelength that yields (c) a maximum in efficiency.

temperature. The shift to a longer transition wavelength allows for a much higher fraction of the incident radiation to be absorbed; when the concentration is large enough, this increase in absorbed energy (along with the decrease in blackbody losses) overcomes the decrease in Carnot efficiency. In short, absorber efficiency trumps Carnot efficiency at high concentrations.

2.6 Non-ideal Surfaces

No surfaces have the ideal step profile considered above. In this section, surfaces with some combination of the properties $a < 1$, $e > 0$, and $w > 0$ (Fig. 2-6) are considered. First the effects of non-zero long-wavelength emission are considered, followed by considerations of the effects of short-wavelength absorptance less than one, and finally the effects of finite-width transitions.

When we consider systems that are not perfect reflectors (i.e. that have non-zero e values), the picture simplifies even further, as only two transition wavelengths are optimal for all concentrations. Figure 2-13 shows the effect of non-zero e values. As the IR emittance increases, the losses in the IR negatively affect system performance, especially at low concentrations. As a result, the optimal operating temperature decreases and the optimal transition wavelength shifts to longer wavelengths.

Selective surfaces that are ideal except that they have short-wavelength absorptance, a, less than 1 do not show much of a change from the ideal selective surface. The ideal operating temperature and transition wavelength are identical, but the system efficiency is reduced. This change in efficiency is plotted in figure 2-14.

In the late 1970s and early 1980s, there was a debate in the literature about what is the minimum width of the transition from high emittance to low emittance[49, 55–57]. Increasing the width of the transition negatively affects the performance at low concentrations, but does not have a large impact at high concentrations. The wide transition causes the amount of radiation absorbed to decrease and the amount of radiation emitted to increase. At high concentrations, the absorbed power is so much larger than the emitted power that this change is not very significant. At

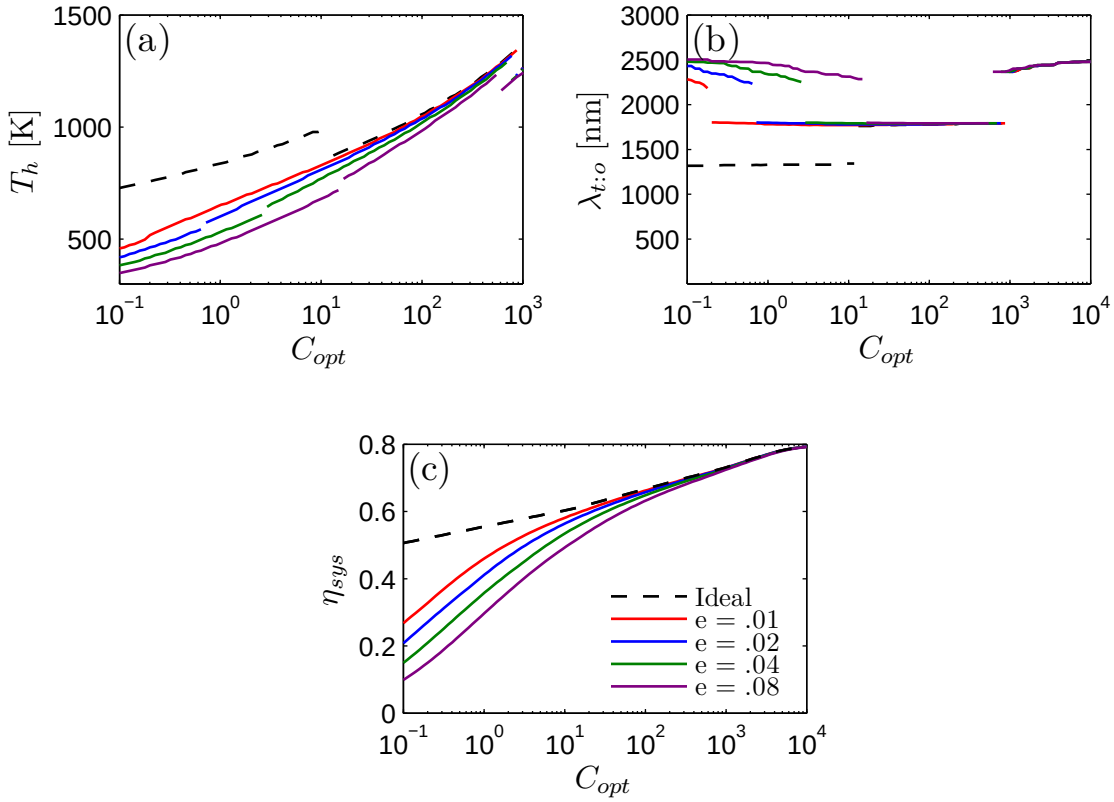

Figure 2-13: Effect of e on system optimization: optimum (a) operating temperature, (b) transition wavelength, and (c) efficiency.

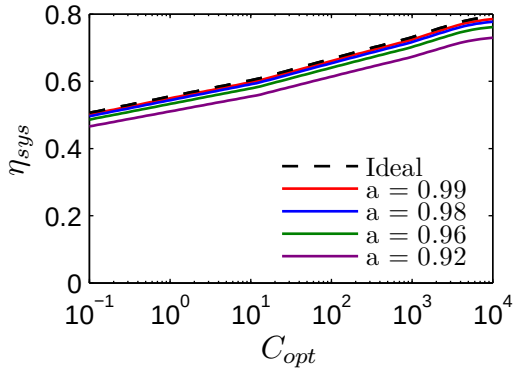

Figure 2-14: Effect of a on maximum system efficiency.

low concentrations, the increase in emitted power is enough to have a large negative impact on the system efficiency. The effect of the width of the transition is shown in figure 2-15.

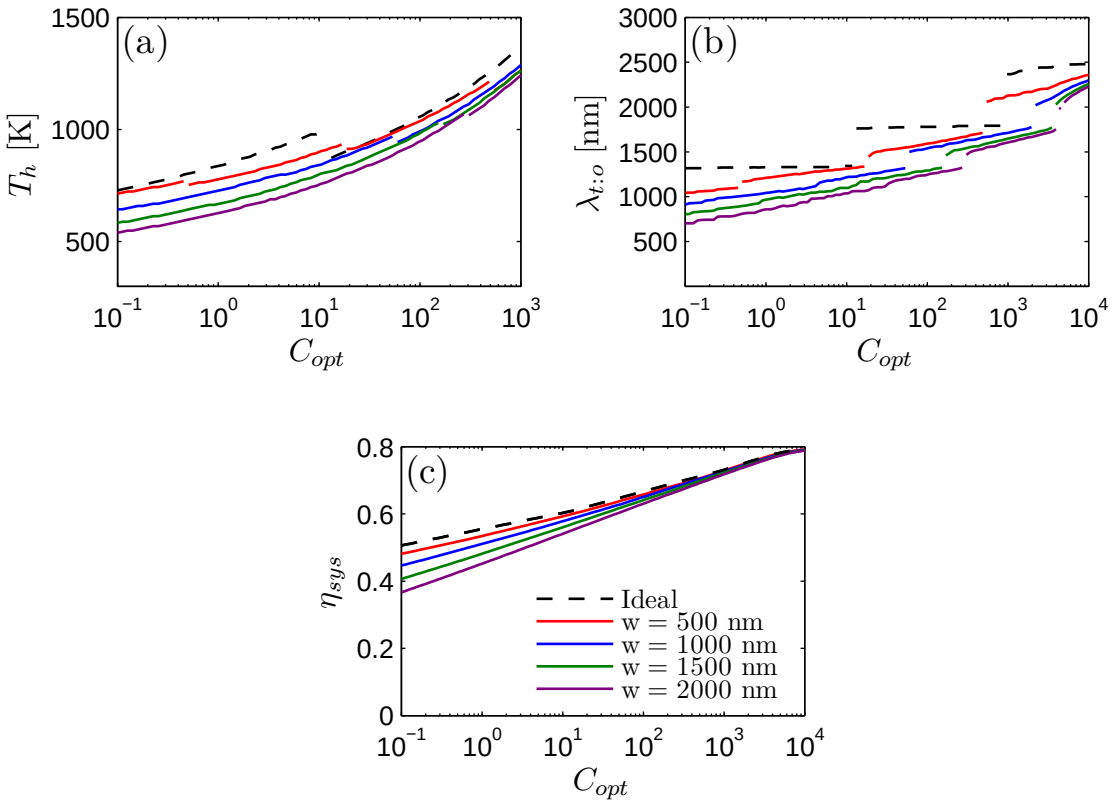

Figure 2-15: Effect of w on system optimization: optimum (a) operating temperature, (b) transition wavelength, and (c) efficiency.

2.7 Improvements

There are three major ways to improve the performance of a selective surface: increasing the visible absorptance, decreasing the IR emittance, and improving the shape of the emittance profile by achieving a sharper transition at the ideal transition wavelength. In order to gauge the value of these improvements to the system efficiency, we use a simplified version of the emittance profile of a commercially-available selective surface as our baseline. The emittance profile consists of a constant value of emittance, a, up to a transition wavelength, λ_t. The emittance then decreases linearly with

wavelength over a width, w, after which it remains at a constant emittance value, e, for all wavelengths greater than $\lambda = \lambda_t + w$. Five test cases are then run: the baseline case, which is defined as $a = 0.95$, $e = 0.03$, $\lambda_t = 1500\,\text{nm}$, and $w = 2000\,\text{nm}$; "Case A," which is the baseline case with an improved short-wavelength absorptance such that $a = 1$; "Case E," which is the baseline case with an improved long-wavelength emittance such that $e = 0$; "Case S," where the values of a and e are the same as in the baseline case but the shape is improved such that λ_t is optimized and $w = 0$; and the ideal case, where $a = 1$, $e = 0$, $w = 0\,\text{nm}$, and the transition wavelength is optimized. These cases are depicted in figure 2-16 and figure 2-17.

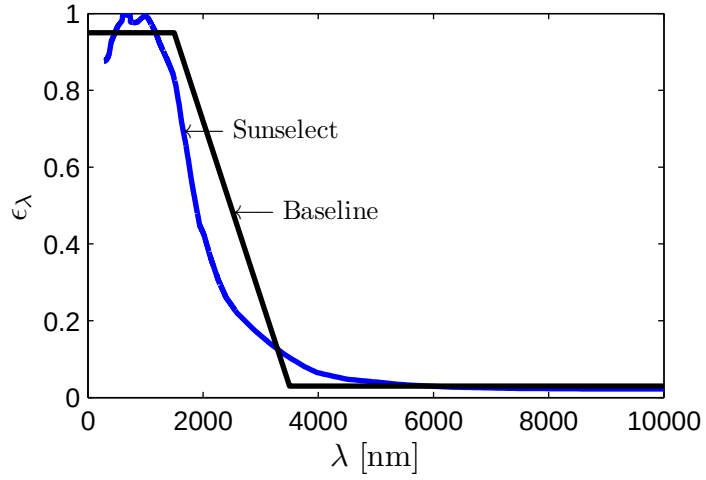

Figure 2-16: Selective surface baseline case, modeled after a commercially-available selective surface (Sunselect® from Alanod). Baseline has properties $a = 0.95$, $e = 0.03$, $\lambda_t = 1500$ nm, $w = 2000$ nm.

The improvements in efficiency are shown in figure 2-18. In the operating regime of flat-panel collectors, the greatest gains in system efficiency come from decreasing the emittance. Emittance dominates the performance in this regime because in order to have high efficiency, the system must operate at higher temperatures. With no concentration, the emission loss at these elevated temperatures dominates because the emission term $\epsilon\sigma_{sb}T^4$ can exceed the solar flux $C_{opt}\,q_{sol}$. The opposite relation is true in the highest-concentration applications, so these applications benefit most from improving the solar absorptance. In the mid-concentration regimes such as where so-

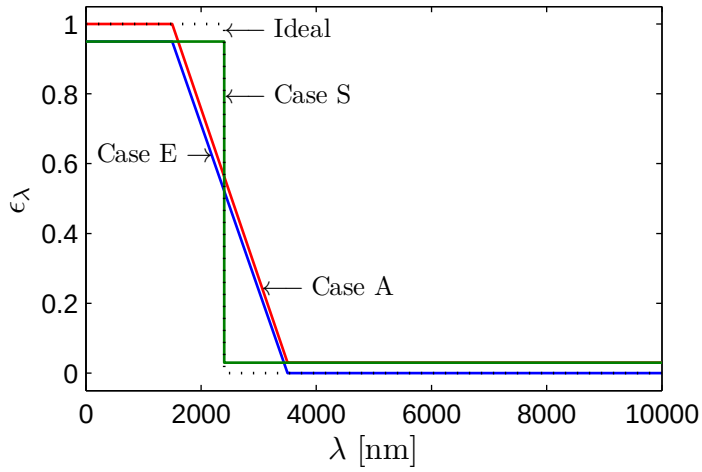

Figure 2-17: Different test cases representing selective surface improvements.

lar troughs operate, the emission and solar flux terms are approximately equal, so improving either has an equal effect on the system efficiency. In effect the total emittance ϵ and the total absorptance α can both be improved just by sharpening the transition between high emittance and low absorptance, hence modifying the shape of the transition without changing the values of a and e can be the most effective modification, especially given the difficulty of achieving surfaces with $\epsilon_\lambda = 1$ or $\epsilon_\lambda = 0$ over a large portion of the spectrum. It is unrealistic to expect materials scientists to ever develop materials with any ideal property $a = 1$, $e = 0$, or $w = 0$; however figure 2-18 shows where certain properties are unimportant: at low concentrations, even the best gains in solar absorptance or transition shape have very little effect on surface efficiency, and at mid- and high-concentrations, decreasing the long-wavelength emittance cannot bring large improvements to system efficiency.

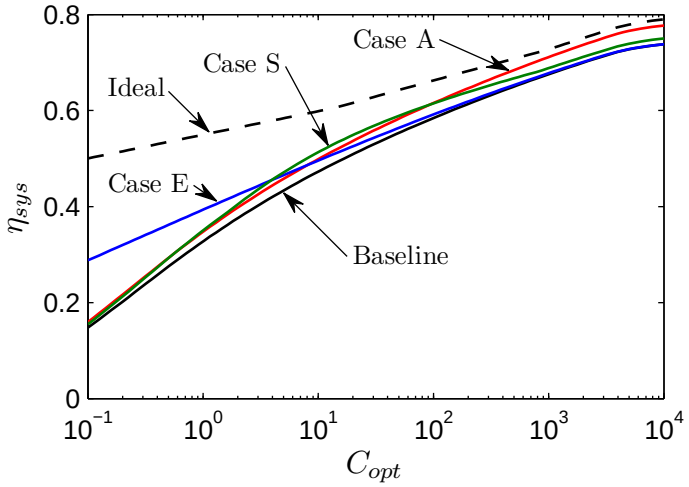

Figure 2-18: System efficiency of a baseline case and four different variations. Case A is increased short-wavelength absorptance; Case E is decreased long-wavelength emittance; Case S is optimized emittance transition.

2.8 Advanced Modeling

In order to more accurately model selective surfaces, more must be known about the surfaces and the system to which it will be attached. System parameters that were ignored in this report include contact resistance, heat losses via conduction and convection, the temperature dependence of the emittance as a function of wavelength, and the temperature dependence of the heat engine performance. Obviously the efficiency of the system would have to be scaled back from Carnot efficiency. It is also important to consider that the solar insolation will fluctuate, although it has been shown that the optimal transition wavelength remains the same for a wide range of solar insolations. An example of advanced modeling follows in Chapter 3, where the system under consideration is a thermoelectric generator. The characteristics of this device, including cycle efficiency as a function of temperature, are calculated in detail. The optimization of selective surfaces for thermoelectric generators is covered in chapter 4.

2.9 Current Materials

Selective surfaces is an active area of research today, with hundreds of papers having been written on the topic. Many surfaces have been developed for applications under 400 °C, yet for concentrating solar power applications including solar thermoelectrics, materials must be developed that have high absorptance and low emittance at higher temperatures[54]. Selective surfaces fall into six broad categories: a) intrinsic, b) semiconductor-metal tandems, c) multilayer absorbers, d) metal-dielectric composite coatings, e) textured surfaces, and f) selectively solar-transmitting coatings on a blackbody-like absorber.[58] These categories will be described below, with examples of the performance of these materials (for a database of the measured or predicted performance of nearly a hundred mid- to high-temperature selective surfaces, see Kennedy's excellent review[54]).

Intrinsic materials are naturally selective bulk materials. Such materials include borides, carbides, and silicides, but even the best of these materials are not excellent selective surfaces: ZrB_2 has a solar absorbtance of only 77% while having an emittance of 8% at 100 °C[59].

Semiconductor-metal tandems are selective surfaces in which the semiconductor absorbs at wavelengths smaller than the bandgap, while the metal substrate has low IR emittance. Germanium oxides on copper substrates have been used for this purpose, acheiving a theoretical solar absorptance of 85% with an emittance of 7.3% at 500 °C[60]. Crystalline and amorphous silicon have also been studied extensively for selective surfaces[48]; Seraphin reports a solar absorptance of 80% with an emittance of 5.7% at 500 °C for a polycrystalline silicon coating on a silver substrate[61]. The high index of refraction causes reflection losses for silicon and germanium surfaces, so many of these systems can be improved with an anti-reflection coating. This stacking of multiple layers leads to the next category of selective surfaces, which is multilayer absorbers.

Multilayer absorbers rely on interference effects between different layers of materials.[62] Two examples of multilayer absorbers are an Al_2O_3-Mo stack, which can

achieve a solar absorptance of 91% and an emittance of 16% at 538 °C, and a MgF_2-Mo-CeO_2 stack, which can achieve a solar absorptance of 85% and an emittance of 6.2% at 538 °C.[63]

Metal-dielectric composite coatings, which are highly absorbing in the solar spectrum yet nearly transparent in the infrared, can be layered on top of a metal substrate to make an effective selective surface. The composite coatings are frequently cermets, which are metal particles in a ceramic (or dielectric) host. The properties of cermets can be tuned via host material choice, particle material choice, particle density, particle shape, particle size, particle structure, particle orientation, and coating thickness.[58] These parameters can be varied throughout the depth of the structure, creating a graded index-of-refraction material. The optimization of these structures is described by Ritchie and Window[64]. As an example, molybdenum/silicon dioxide cermets have been measured with a solar absorptance of 94% and an emittance of 13% at 580 °C[65].

Textured surfaces can also act as selective absorbers. These surfaces rely on geometric, porous, or dendritic structures, which have features small enough so that they appear rough to short-wavelength radiation and smooth to long-wavelength radiation. The short-wavelength light is more effectively absorbed by the multiple reflections created by the structures, while the long-wavelength radiation is essentially unaffected by the surface features. Dendritic tungsten has been shown to have 96% absorptance and 26% emittance at 550 °C[66].

The sixth category of selective surfaces is selectively solar-transmitting coatings on blackbody substrates. These systems allow the solar radiation to transmit through the coating and be absorbed by the blackbody, while preventing the transmission of IR losses from the blackbody. Examples include gold films on glass, where the gold film is encapsulated by titanium dioxide short-wavelength antireflection coatings, and doped oxide-semiconductor coatings. An example of a doped oxide-semiconductor coating is aluminum-doped zinc oxide, which as a film has a visible transmittance of 99% and an infrared reflectance of 85%[67].

Development continues on all of these material fronts. Ideally, the development of

these materials would begin by identifying the ideal transition wavelength for these materials based on the thermal stability range of the material system and the minimum predicted long-wavelength emittance. When this is accomplished, the materials systems can be tuned to achieve the ideal transition wavelengths. In addition, the performance benefits of modifying the emittance curve can be calculated such that the development of selective surfaces will be driven towards producing the best possible thermal energy conversion system.

2.10 Conclusion

This chapter outlined a methodology for analyzing selective surfaces. Although the ideal selective surface is impossible to obtain, the models presented here can give an engineer a good grasp as to what parameters are important for his or her application. For high-concentration applications, the focus should be on improving the visible absorptance. For mid-concentration applications, the focus should be on improving the shape of the transition. For non-concentrating applications, the focus should be on decreasing the IR emittance. It should be noted that there exist two key transition wavelengths: 1750 nm for mid-concentration systems operating at approximately 900 K; and 2400 nm for both non-concentrating and high-concentration systems. Researchers and entrepreneurs alike can use the basic conclusions to see opportunities for areas of improvement in current selective surface technology. There is also a conclusion that a thermal engineer or systems engineer should note: this chapter describes upper limits for the working temperatures of solar-powered cycles. Figure 2-10 clearly shows that exceeding the optimal temperature results in a decrease in system performance. For Carnot cycles or systems that operate at a constant fraction of Carnot, the value of this temperature is shown in figure 2-12(a). For other systems, this calculation should be performed with the performance characteristics of the cycle programmed into the algorithm.

Chapter 3

Solar Thermoelectric Generators

This chapter describes modeling the conversion of solar energy into electricity via the thermoelectric effect. Previous terrestrial solar thermoelectric generators (STEGs) have only achieved efficiencies below 4% at optical concentration ratios of less than 75X, typical of a parabolic trough. These STEGs were missing key efficiency-boosting parameters; the model presented here suggests that a design comprising existing high-performance thermoelectric materials, an existing low-emittance selective surface, and a vacuum environment can approach 13% efficiency, comparable to the highest-performing dye-sensitized photovoltaic cells.

This chapter begins with a review of previous work on STEGs, followed by a description of the method of numerically modeling STEGs. To model STEGs, first a single p-type or n-type leg is modeled. Then a thermoelectric pair comprising one p-type and one n-type leg is modeled and optimized for efficiency. Next, thermoelectric devices comprising multiple thermoelectric materials are modeled. To model solar thermoelectrics, the thermoelectric device models can be combined with an energy balance on the selective surface. For multi-material solar thermoelectrics, an energy balance must also be performed on the midplane that joins the upper stage to the lower stage, as this midplane acts as a radiation shield between the hot side and the cold side. The efficiencies of these STEGs are calculated over a range of incident fluxes from $100\,\mathrm{W\,m^{-2}}$ to $1000\,\mathrm{kW\,m^{-2}}$, encompassing everything from non-concentrating systems to solar towers. These calculations of performance of solar thermoelectric

generators are followed by an analysis of the system-level benefits of thermoelectric and selective surface improvements, specifically how the emittance of the selective surface and thermal conductivities of the thermoelectric materials can enhance the STEG performance. This chapter ends with a summary of the completed STEG modeling.

3.1 History of Solar Thermoelectric Generators

The concept of using the sun's heat to power a thermoelectric generator is not new; a century of various STEG experimental and modeling efforts can be found in the literature. Edward Weston received his first US patent for solar thermoelectric generators in 1888[68]. In 1913, Coblentz received a patent for a solar thermoelectric generator which included the possibility of using optical concentration[69], although he does not predict that optical concentration would lead to increased efficiency. Coblentz built this device, but he managed to measure an efficiency of less than one hundredth of one percent. In 1954, Maria Telkes published the first well-documented results of a solar thermoelectric generator whose efficiency was on the order of one percent[70]. She measured 0.63% solar-to-electrical efficiency under no optical concentration using ZnSb p-type elements and doped Bi_2Te_3 n-type elements. When she applied optical concentration to her system, she was able to measure an efficiency of 3.35%. This is a good result given that Telkes used a non-selective surface, her system was not in vacuum, and her thermoelectric materials had an effective ZT of approximately 0.3 operating between 200 °C and 20 °C.

The period after Telkes' publication is marked by the rapid advancement of the US space program. During this time, various authors published technical reports and papers about the use of solar thermoelectric generators in space. Since these devices would operate in the nearly perfect vacuum of space, there would be no convection losses. A research program at the General Instrument Corporation designed and built solar thermoelectric generators for space[71, 72]. They predicted an efficiency of 3.8% at AM0 conditions, and were able to achieve approximately 30% of this value in a lab

experiment. A similar program at the Radio Corporation of America (RCA)[73, 74] designed a space-based STEG to be operated at 0.25 AU (one astronomical unit, AU, is the mean distance from the sun to the earth, or approximately 160 million kilometers). At 0.25 AU, the solar flux is more than $22\,\mathrm{kW\,m^{-2}}$. They predicted an efficiency of only 3.6% for their device. During this time, Fuschillo *et al.* and Fuschillo and Gibson published papers[75, 76] describing the performance of space-based STEGs. They predicted an efficiency of 4.2% and although their experiment could not test this efficiency, they did have success in matching the thermoelectric performance data to their model.

The next wave of thermoelectric generator research occurred in the late 1970s and early 1980s, most likely as a repsonse to the energy crises of the 1970s. In 1980 Goldsmid *et al.* published results on earth-based STEGs[77]. Despite using some optical concentration (less than 3X), Goldsmid *et al.* predicted an efficiency of less than one percent, most likely because they did not enclose their system in a vacuum. Their measured efficiency was only 40% of their predicted efficiency. While Goldsmid *et al.* focused on low-concentration applications, Rowe published theoretical results for high-concentration earth-based STEGs[78]. Rowe calculated that using silicon germanium thermoelectrics, the STEG efficiency would approach 12% as optical concentration approached 2000X. Various papers on STEGs[79–81] were also published in the early 1980s, however their lack of details (and unimpressive performance) limited their influence on the field. In 1984, Lidorenko *et al.* published modeling and experimental results of an earth-based STEG[82]. Their system comprised a selective surface and high-performance bismuth and antimony thermoelectric materials inside a vacuum enclosure without optical concentration. They report an efficiency of 3.7%, but this number is impossible given the materials and setup that they described. Most likely, the inflated results were due to them not directly measuring the incident flux, especially since they used an uncalibrated light source instead of a calibrated solar simulator. Despite their questionable results, their paper is worth mentioning since they do take the proper approach to solar thermoelectrics by using thermal concentration along with high-performance materials. Since the publication of Lidorenko

et al., which is almost never cited by the English-speaking thermoelectrics community, most STEG development continued to focus on either space-based STEGs, or on earth-based STEGs with optical concentration.

After the mid-1980s, there was little published solar thermoelectric research until the early twenty-first century, most likely as a byproduct of the advances in thermoelectrics spawned by the works of Hicks and Dresselhaus[25, 26]. The space-based STEG work occurred under the support of the European Space Agency as part of a study for a mission to Mercury: Scherrer *et al.*[83] predicted a STEG could produce 6.9% efficiency at 0.45 AU ($6.7\,\mathrm{kW\,m^{-2}}$). Rockendorf *et al.*[84] published a paper on hybrid systems, where the waste heat from the cold side of STEGs could be used as a domestic hot water source. Micro-power generators were analyzed and tested[85, 86], including a design where STEGs were used in conjunction with phase-change materials in an attempt to provide power both day and night[87, 88]. These designs reached efficiencies of at best 3.0% at 66 suns concentration[86]. Most of the papers cited here use simplified models that do not capture the true effects happening inside the thermoelectric materials. The simplified models overestimate the performance of STEGs, especially at higher temperatures, and also can ignore the temperature-dependence of the materials. For example, one oft-cited paper[89] uses over-simplified models of thermoelectrics to predict that bismuth telluride STEGs can reach over 50% efficiency at temperatures approaching 1000 K - four hundred degrees above the melting point of this material. This thesis will focus on the accurate modeling of high-concentration solar thermoelectric models. The assumptions that are made are explicitly listed in the following section.

3.2 Modeling Assumptions

In the models in this paper, the following assumptions and approximations are made:

- *The material properties are only a function of temperature, not position.* This assumption is not true if there is diffusion of species near the boundaries of the thermoelectric material, or if the material is not homogenous when manufac-

tured. Thermoelectric legs in which the chemical composition is intentionally varied as a function of position are called functionally graded materials[90].

- *There is no thermal or electrical contact resistance.* This assumption yields the maximum performance of the device. For high-performance devices, contact resistances must be minimized. If the contact resistances are significant and well-characterized, they can be included in the advanced model discussed in section 5.2.

- *The radiation losses from the edges of the collector are ignored.* The thickness of the collector is normally less than 0.5 mm, which is smaller than our collector length and width tolerances. In addition, it is likely that mass-produced solar thermoelectric generators would have many thermoelectric couples attached to a single large collector, thus reducing the effect of these small edge areas.

- *There are no convection losses from the thermoelectric legs or the collector.* Convection can be eliminated by enclosing the system in a vacuum.

- *The radiation exchange involving the legs is ignored.* Radiation from the collector to the legs is small enough to be ignored, which means the total heat input into the thermoelectric is just the Peltier and Fourier heat at the interface. Similarly, radiation losses from the legs are small enough to be ignored. This assumption is validated by calculations made by Kraemer, to appear in his Ph.D. dissertation.

- *The temperature, heat flux, and electric current in the leg do not vary across the cross-section of the leg.* At both the hot-side and cold-side interfaces, the electric current and heat flux is assumed to be spread evenly across the leg. Sidewall radiation losses will produce some nonuniformity in the temperature from the center of the leg to the leg surface. These losses could be modeled with an average linearized heat transfer coefficient of $25\,\mathrm{W\,m^{-2}\,K^{-1}}$. Hogan and Shih[91] showed that losses of this magnitude are small with legs on the order of 1 cm; given that the length of the legs used in this thesis are on the

order of 1 mm, the losses should be even smaller and thus it should be safe to model the heat flux in the leg as one-dimensional.

- *The temperature of the collector is uniform.* This is a reasonable assumption, proved by Kraemer[92].

- *The cold side can be maintained at a fixed temperature T_c.* If the cold side varies as a function of heat flux, then the results from the model presented in this thesis can be inserted into a more comprehensive system model.

- *At low optical concentrations, the area of the collector is much greater than the cross-sectional area of the leg.* This allows setting the radiating area of the back side of the collector equal to the radiating area of the front side of the collector, which results in the efficiency of the collector being independent of the size of the thermoelectric material geometry. For the non-concentrated solar themoelectrics considered in this thesis, the area of the legs is usually less than 0.5% of the area of the collector. At low thermal concentrations which correspond to high optical concentrations, the back-side radiating area is significantly smaller than the front-side radiating area because the cross-sectional area of the legs is relatively large. When the true collector back-side radiating area is calculated, the efficiency of the collector is not independent of the thermoelectric geometry. However, it will be shown that when the optical concentration is high, the losses from the back side of the collector become very small relative to the overall heat flux, and thus even in these cases equating the front-side area to the back-side area has very little effect on the predicted efficiency of the system.

- *The cross-sectional area of a thermoelectric leg is constant along the leg.* Varying the cross-sectional area can benefit systems with contact resistance or radiation losses. Given the small size of the thermoelectric elements used in this thesis, it is reasonable to assume they would be manufactured with a constant cross-sectional area down the leg.

3.3 Thermoelectric Modeling

This section describes the modeling of a thermoelectric element of length L and cross-sectional area A, shown in figure 3-1. As mentioned before, it is assumed that the thermoelectric element is made of only one material and that there is no variation in composition as a function of position, so that the Seebeck coefficient, $S(T)$, electrical conductivity, $\sigma(T)$, and thermal conductivity, $\kappa(T)$, are only a function of temperature, not position. In addition, it is assumed that the radiation and convection losses from the element are negligible. Therefore, the leg is modeled as a one-dimensional system in which the energy flux in the x-direction is conserved.

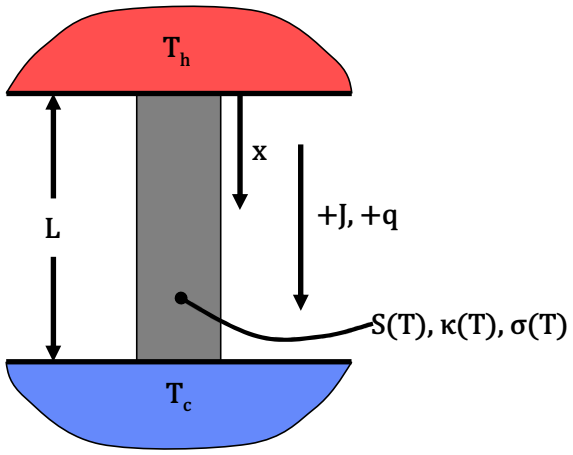

Figure 3-1: Model for one-dimensional flow in a single TE leg between two heat reservoirs at T_h and T_c.

The foundation of thermoelectric device modeling was laid by Charles Domenicali in 1953 with his paper on the irreversible thermodynamics of thermoelectrics[93]. From the work of Callen[94] and deGroot[95] built on the Onsager reciprocal relations[96, 97], Domenicali describes three fundamental relations of thermoelectrics:

$$J^s = S^* J^e - (\kappa/T)\,\nabla T \tag{3.1}$$

$$W = (TS^* + \bar{\mu})\,J^e - \kappa \nabla T \tag{3.2}$$

$$\nabla \bar{\mu} = -e^2 \rho J^e - S^* \nabla T \tag{3.3}$$

The first equation describes the entropy current density, J^s, as the sum of the transport entropy and the heat flux entropy, where S^* is the transport entropy per particle, J^e is the particle current density, κ is the thermal conductivity, and T is the temperature. The energy current density, W, is the sum of the particle current energy and the heat flux due to the temperature gradient. The electrochemical potential, $\bar{\mu}$, comprises a chemical part, μ, and an electrical part: $\bar{\mu} = \mu + e\phi$, where e is the magnitude of the charge of an electron and ϕ is the electrostatic potential[94]. The change in electrochemical potential is the negative of the sum of the Ohmic voltage and the thermoelectric voltage. Here it is helpful to use charge instead of particles, so the following substitutions are made: the electromotive force, $V = \bar{\mu}/(-e)$; the charge current density, $J = -eJ^e$; and the Seebeck coefficient, $S = S^*/(-e)$. Equations (3.1) - (3.3) can be rearranged as follows:

$$q = TJ^s = TSJ - \kappa\nabla T \tag{3.4}$$

$$W = (TS + V)\,J - \kappa\nabla T \tag{3.5}$$

$$\nabla V = -\rho J - S\nabla T \tag{3.6}$$

Here q is the heat current density, a combination of the thermoelectric heat (TSJ) and the Fourier heat. An energy balance on a slice of the leg of length Δx is shown in figure 3-2. If the system is at steady state, then the energy current density in, W_x, must be equivalent to the energy current density out, $W_{x+\Delta x}$. Taking the limit as $\Delta x \to 0$ and rearranging, we find that the total energy generated in the differential volume is the sum of the Thomson heat and the Joule heat (Eq. (3.7)).

$$\kappa\nabla^2 T = JT\frac{dS}{dT}\nabla T - \rho J^2 \tag{3.7}$$

The heat flux and temperature along a thermoelectric element can be computed by first solving the second-order differential equation for T (Eq. (3.7)) and then differentiating the temperature profile to find the heat flux (Eq. (3.4)). This method is difficult to do numerically if the temperature dependence of the material properties

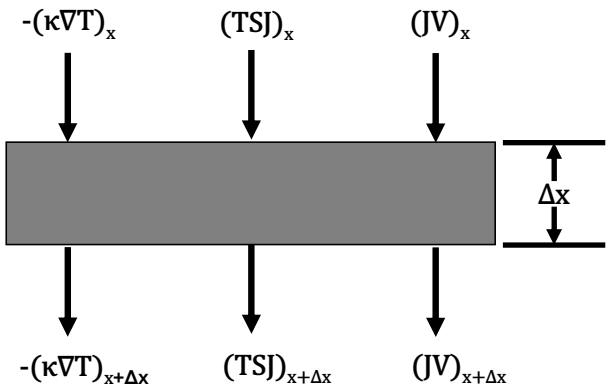

Figure 3-2: Energy balance on a differential slice of a thermoelectric leg.

is not ignored. A simpler numerical method is to rearrange Domenicali's equations (Eqs. (3.4), (3.5), (3.6)) into a pair of coupled differential equations. The first equation is attained by solving equation (3.4) for the temperature gradient; the second is attained by substituting equation (3.4) into equation (3.5), setting the derivative equal to zero, and substituting equation (3.6):

$$\frac{dT}{dx} = \frac{TSJ - q}{k} \tag{3.8}$$

$$\frac{dq}{dx} = \rho J^2 + SJ\frac{TSJ - q}{k} \tag{3.9}$$

The first equation tells us that the temperature gradient equals the conduction heat flux divided by the thermal conductivity of the material; the second equation equates the heat flux out of a volume to the sum of the Joule heat and Thomson heat generated in the volume. Again these equations require that there are no other heat fluxes from the differential element, such as radiation or convection losses.

These equations can be used to calculate the state of a thermoelectric leg of length L operating between two heat reservoirs, $T_{x=0} = T_h$ and $T_{x=L} = T_c$. Besides the temperatures of the heat reservoirs, either the external load resistance or the current through the leg must also be known. We will perform calculations through the leg using the current as the independent variable; if desired, the external load resistance can be calculated by dividing the output voltage by the current. We solve the coupled

differential equations (Eqs. (3.8) and (3.9)) by choosing a current, guessing an initial heat flux $q_{x=0}$, calculating the resulting temperature and heat flux profiles in the leg, and then adjusting the guess of the initial heat flux until the temperature at the end of the leg matches the temperature of the cold-side heat reservoir.

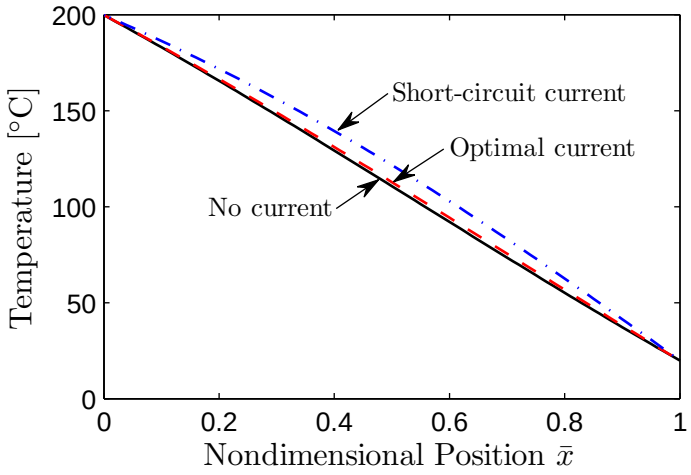

Figure 3-3: Temperature profile within a p-type Bi_2Te_3 thermoelectric leg at zero current, short-circuit current, and current at maximum efficiency.

As an example, the temperature and heat flux profiles are calculated for a p-type Bi_2Te_3 sample with properties from figure A-2, operating between two heat reservoirs at 200 °C and 20 °C. The profiles are plotted in figure 3-3. This thermoelectric leg extracts electrical power from the temperature gradient. Since energy is conserved in the x-direction, the electrical power P_{el} is the difference of the heat flows at each end of the leg:

$$P_{\mathrm{el}} = I\Delta V = I\left(V_c - V_h\right) = A\left(q_h - q_c\right) \tag{3.10}$$

The efficiency of the thermoelectric leg, η_{leg}, is defined as the electrical power divided by the heat input. Since radiation from the collector to the leg is very small, the heat input can be approximated by the heat (Peltier and Fourier) at the hot side of the leg:

$$\eta_{leg} = \frac{P_{el}}{Q_h} = \frac{q_h - q_c}{q_h} \tag{3.11}$$

In order to better understand thermoelectric power generation, to predict the effectiveness of segmented thermoelectric legs, and to make geometry-independent models for streamlined calculations, it is useful to define two important parameters: the thermoelectric potential and the relative current density.

3.3.1 Thermoelectric Potential and Relative Current Density

The ability of a thermoelectric leg to convert heat to electricity is a function of the material properties and the boundary temperatures. It is also a function of the relative quantity of electric current flowing down the leg. Snyder and Ursell[98] define the ratio of the heat flux to the electric current density as the thermoelectric potential, Φ:

$$\Phi = \frac{q}{J} = \frac{W}{J} - V \tag{3.12}$$

In this one-dimensional model, both energy and electric current are conserved in the x-direction, so the term W/J is constant. It is then clear from equation (3.12) why Φ is called the thermoelectric potential: the change in Φ is just the negative of the change of the voltage in the material. It follows from equation (3.12) that the heat current density at any point in the thermoelectric leg is the product of the thermoelectric potential and the electric current density:

$$q = J\Phi \tag{3.13}$$

There is then one more way to define the power and efficiency of a thermoelectric leg:

$$\eta_{leg} = \frac{P_{el}}{Q_h} = \frac{I\Delta V}{Q_h} = \frac{J\left(V_c - V_h\right)}{q_h} = \frac{q_h - q_c}{q_h} = \frac{\Phi_h - \Phi_c}{\Phi_h} \tag{3.14}$$

As it is the balance of the total heat current to the electrical current, the thermoelectric potential can be thought of as a tuning parameter to maximize the per-

formance of a thermoelectric leg. From equation (3.14), we can see that the thermoelectric potential must vary down the length of the leg if the leg is to deliver electric power. Most of this variation comes from the changing thermoelectric heat term. As seen in figure 3-3, the temperature gradient changes little down the leg, so the Fourier heat changes little. As a result, the ratio of the electric current to the Fourier heat is nearly constant along the leg. Snyder and Ursell call this ratio the relative current density, u:

$$u = \frac{J}{-\kappa \nabla T} \tag{3.15}$$

$$\Phi = ST + \frac{1}{u} \tag{3.16}$$

With these definitions the coupled differential equations (Eqs. (3.8) and (3.9)) can be rewritten as:

$$\frac{dT}{dx} = \frac{TS - \Phi}{k} J \tag{3.17}$$

$$\frac{d\Phi}{dx} = \left[\rho + S\frac{TS - \Phi}{k}\right] J \tag{3.18}$$

For a differential element over a small ΔT such that the material properties can be assumed to be constant, the efficiency of the thermoelectric element is:

$$\eta = \frac{-\Delta\Phi}{\Phi_h} = \frac{\left[\rho + S\frac{T_h S - \Phi_h}{\kappa}\right] J\Delta x}{\Phi_h} \tag{3.19}$$

$$\eta = \frac{-\Delta T}{T_h} \cdot \frac{\left[\rho + S\frac{T_h S - \Phi_h}{\kappa}\right] \frac{J\Delta x}{\Delta T}}{\Phi_h / \Delta T} \tag{3.20}$$

The first term in equation (3.20) is the Carnot efficiency; the second term is the reduced efficiency, η_r. After simplifying, the reduced efficiency is expressed as:

$$\eta_r = \frac{S - u\rho\kappa}{S + \frac{1}{uT_h}} \tag{3.21}$$

At a given temperature, the value of u that maximizes the reduced efficiency is called

the compatibility factor, s:

$$s = \frac{\sqrt{1+ZT}-1}{ST} \tag{3.22}$$

It has already been shown that the relative current density changes little along the length of a thermoelectric leg. To see if a material is self-compatible, *i.e.* if the same current density is optimal for the entire leg, one can calculate the compatibility factor for the the material. If a material has a constant compatibility factor, each differential element of the leg will be operating as efficiently as possible. Materials that have widely varying compatibility factors must have portions of the leg that are not operating at their maximum efficiency, so the overall efficiency of the leg is smaller than the efficiency of a leg with an identical ZT but with a constant compatibility factor. An extended discussion on the efficiency as a function of compatibility factor was written by Snyder[99]. Figure 3-4 shows the compatibility factor for the p- and n-type bismuth telluride and skutterudite materials used in this thesis. The skutterudite materials are much more self-compatible than Bi_2Te_3 materials. Luckily for both p-type and n-type legs, the compatibility factor of Bi_2Te_3 is not far from the compatibility factor of skutterudites. This fact becomes evident in subsection 3.5.1.

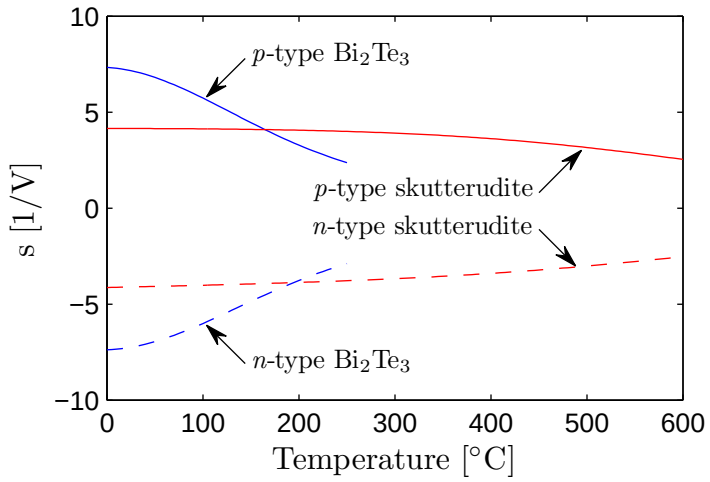

Figure 3-4: Compatibility factor of Bi_2Te_3 and skutterudite materials.

3.4 Device Modeling and Optimization

It is possible to optimize a STEG by varying all the possible parameters and finding a global maximum in efficiency. However, this approach can be computationally-intensive and is not modular. In this thesis, the STEG is broken into modular units whose performance characteristics can be calculated in advance and then fed into an optimizing algorithm. With this method, very little has to be recalculated if one parameter of a system is changed. For example, if the emittance of the selective surface changes, only the new selective surface performance needs to be calculated; there is no need to recalculate the performance of the thermoelectric legs. The models also reduce the system to just a few dimensional parameters, which limits the degrees of freedom of the model and hence reduces the amount of calculation required. The first model that is optimized is a single thermoelectric leg. Next, a thermoelectric generator (TEG) comprising one p-type and one n-type leg is modeled. The concept of a TEG is extended to multi-material TEGs covering large temperature drops. Finally, TEGs are combined in a vacuum with a solar collector to form a STEG.

3.4.1 Leg Optimization

When a thermoelectric leg of fixed geometry operates between two heat reservoirs at fixed temperatures, the electric current must be optimized to yield maximum device efficiency. As an example, we calculate the efficiency of a p-type Bi_2Te_3 thermoelectric leg, whose properties are shown in figure A-2, operating between two heat reservoirs at $T_h = 200\,°C$ and $T_c = 20\,°C$. The leg is a $1\,mm \times 1\,mm \times 1\,mm$ cube. The efficiency of this device is optimized by sweeping through a range of electric currents (up to the short-circuit electric current, I_{sc}); calculating the necessary hot-side heat flux, Q_h, to satisfy the boundary conditions; calculating the electrical power; and then calculating the efficiency. This process is illustrated in figure 3-5. It is important to note that as the electric current increases, the Joule heating within the sample increases, but in most thermoelectrics the temperature profile changes very little with increasing electrical current (Fig. 3-3) because the term $I_{sc}^2\rho/\kappa$ is small.

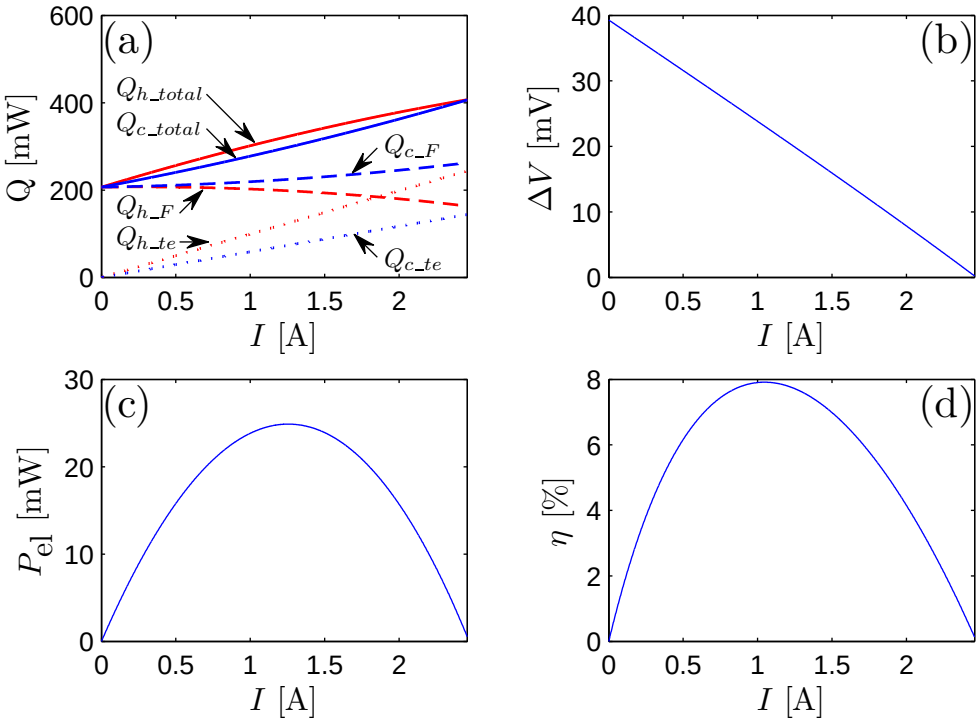

Figure 3-5: Performance of a thermoelectric device over a fixed temperature range as a function of electric current. (a) Hot-side and cold-side total heats are the sum of the Fourier and thermoelectric heats, (b) output voltage, (c) power, (d) efficiency.

In figure 3-5(a), the heat transferred (absorbed or released) at each end of the device varies as a function of the electric current. The heat (solid) is the sum of the Fourier heat, $-\kappa\nabla T$ (dashed), and the thermoelectric heat, TSJ (dotted). The Fourier heat falls off slowly as a function of current because of the small change in the temperature profile within the leg. The heat divided by the electric current yields the thermoelectric potential at both ends of the leg. The output voltage (Fig. 3-5(b)), which is the change in the thermoelectric potential, decreases nearly linearly with increasing electric current. The reason becomes clear when the output voltage is expressed as the Seebeck voltage minus the Ohmic voltage:

$$\Delta V = \int_{T_c}^{T_h} S(T)dT - \frac{I}{A}\int_0^L \rho(T)dx \tag{3.23}$$

The nonlinearity of this equation comes from the second term: as the current increases, the increase in the temperature profile increases the electrical resistivity. However, this effect is very small, as seen in figure 3-5(b). Multiplying the output voltage times the electric current yields the electrical power, P_{el}, seen in figure 3-5(c). Finally the efficiency is found from figure 3-5(d). Note that the maximum efficiency occurs at a lower electric current than the maximum power. The results of a calculation for a given geometry (such as the preceding example) can be scaled to give the performance for a different geometry. At this point it is instructive to rewrite equations (3.17) and (3.18) by nondimensionalizing the x position and scaling the electric current, the heat flux, and the electric power by the leg length:

$$\bar{x} = x/L \tag{3.24}$$

$$\widetilde{I} = JL = I\frac{L}{A} \tag{3.25}$$

$$\widetilde{Q} = qL = Q\frac{L}{A} \tag{3.26}$$

$$\widetilde{P_{\mathrm{el}}} = P_{\mathrm{el}} \frac{L}{A} \tag{3.27}$$

$$\frac{dT}{d\bar{x}} = \frac{TS - \Phi}{k} \widetilde{I} \tag{3.28}$$

$$\frac{d\Phi}{d\bar{x}} = \left[\rho + S \frac{TS - \Phi}{k} \right] \widetilde{I} \tag{3.29}$$

From these equations it is clear that the important geometric parameter is not the length or the area, but the ratio of the length to the area, L/A. For example, doubling both the length and the area of a thermoelectric sample will have no effect on its performance (advanced modeling with radiation losses, convection losses, and contact resistance will suggest otherwise, but it is a valid approximation for the systems studied here). It is very important to realize that since the temperature is fixed at both boundaries, there is only one independent variable in the problem: that is, for each $\widetilde{I}$, there is a corresponding Φ profile. One only needs to choose I and the ratio L/A to fully constrain the problem. Intuitively, setting L/A and I is analogous to setting the resistance of the thermal circuit ($\sim L/\bar{\kappa}A$) and the resistance of the electrical circuit (adjusted to yield a given I). This ability to scale a given solution allows for much faster computation. It also provides insight into how geometric parameters affect the operation of thermoelectric generators.

3.4.2 Optimization of a *p*-*n* Pair

For a thermoelectric device to generate electricity there must be a closed electrical circuit where current flows in a loop (or loops) between the hot side and cold side of the device. A single n-type or p-type leg is not sufficient; there must be a pair of thermoelectric materials together. When operating a pair of thermoelectric materials, it is easy to adjust the area of each leg such that each leg operates at its maximum efficiency. However, this will not be the optimal operating point for the pair unless the legs have identical efficiencies. The optimization of a pair of thermoelectric elements

is easy with the thermoelectric potential. The efficiency of the TEG is the total electrical power delivered divided by the total power absorbed at the hot side:

$$\eta_{TEG} = \frac{P_{el}}{Q_{abs}} = \frac{\eta_n Q_{h,n} + \eta_p Q_{h,p}}{Q_{h,n} + Q_{h,p}} = \frac{\eta_n \Phi_{h,n} + \eta_p \Phi_{h,p}}{\Phi_{h,n} + \Phi_{h,p}} \tag{3.30}$$

If the analysis has been done for each leg over a given temperature drop, then these functions for Φ_h and η as functions of $\widetilde{I}_n$ and $\widetilde{I}_p$ can be inserted into the above equation. For two legs with different efficiencies, it is preferred if the leg with higher efficiency has a larger magnitude Φ_h so that more heat is converted to electricity by this more efficient leg, even if the leg itself is not operating at its peak efficiency. In the end, neither leg will operate at its optimal (Φ_h, $\widetilde{I}$) condition: the leg with lower efficiency will run smaller than optimal Φ_h and the leg with higher efficiency will run larger than optimal Φ_h so that a larger fraction of heat will be converted by the more efficient leg. This effect tends to be small, especially if the materials are relatively well-matched in terms of efficiency. For a Bi_2Te_3 pair with the material properties shown in figures A-1 and A-2 operating between 200 °C and 20 °C, the materials are well-matched: the p-type leg can reach 7.9% efficiency and the n-type leg can reach 7.6% efficiency. Paired together, the p-type leg runs at 101% of its individual optimal Φ_h, while the n-type leg runs at 99% of its individual optimal Φ_h, for a combined efficiency of 7.8%. For a skutterudite pair with the material properties shown in figures A-3 and A-4 operating between 600 °C and 200 °C, the materials are not as well-matched: the p-type leg can reach 8.3% efficiency and the n-type leg can reach 9.7% efficiency. Still, when paired together the p-type leg runs at 97% of its individual optimal Φ_h, while the n-type leg runs at 103% of its individual optimal Φ_h, for a combined efficiency of 9.1%.

The properties Φ and $\widetilde{I}$ can also be defined for a thermoelectric p-n pair, based on the total cross-sectional area of the legs. Both Φ and $\widetilde{I}$ are only meaningful if the ratio of the n-type leg cross-sectional area to the p-type leg cross-sectional area, $R_{n/p}$ is known.

3.5 Multi-Material Thermoelectrics

Most thermoelectric materials have a high ZT (approaching or exceeding unity) for only a small portion of the temperature range in which they can operate (Fig. 3-6). When thermoelectric generators span large temperature drops, it is beneficial to use multiple materials, with one thermoelectric material generating electricity between the hot side and an intermediate temperature, and a second thermoelectric material generating electricity between the intermediate temperature and the cold side. In this study, the materials used for upper and lower temperature ranges are skutterudite materials and bismuth telluride materials, respectively. Their material properties can be seen in figures A-1, A-2, A-3, and A-4. There are two main strategies[100] for splitting the temperature range with two materials: segmented thermoelectrics and cascaded thermoelectrics. These designs are explained in the following subsections.

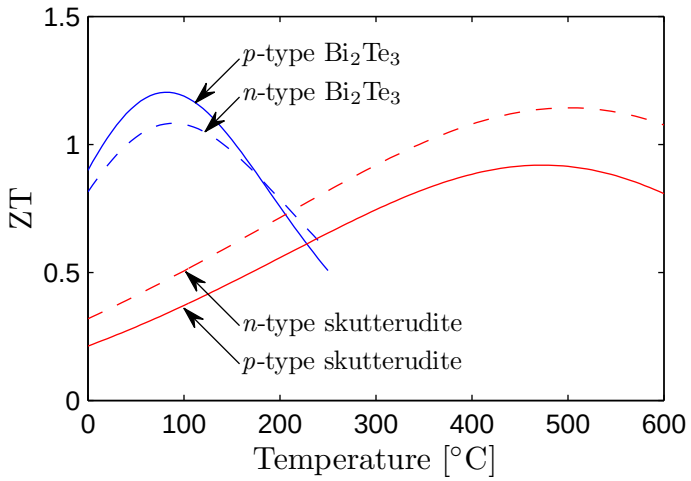

Figure 3-6: Dimensionless figures of merit ZT of p-type and n-type Bi_2Te_3 and skutterudite materials.

3.5.1 Segmented Thermoelectrics

Segmented thermoelectric devices use two thermoelectric materials pressed into a single leg. For example, an n-type segmented thermoelectric leg could consist of an n-type skutterudite leg fused to an n-type bismuth telluride leg; the p-type leg would

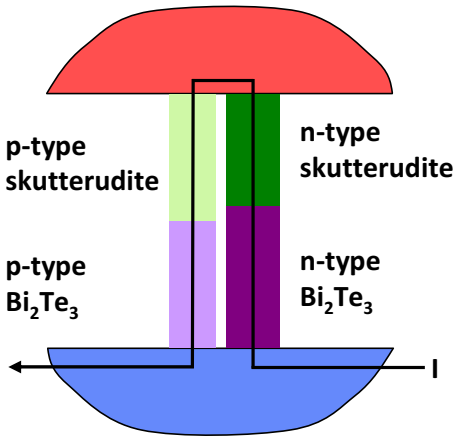

Figure 3-7: A segmented thermoelectric generator.

be similar. This architecture is shown in figure 3-7. This is the simplest architecture for a multi-material thermoelectric generator because there is only one current loop through the device, and there are an equal number of skutterudite segments as Bi_2Te_3 segments. The boundary conditions at the interface between the upper and lower material in the leg require that the heat and the current must be conserved. Since the thermoelectric potential is the ratio of the heat to the current, it too must be continuous at the boundary: $\Phi_{mid,upper} = \Phi_{mid,lower}$. This rigid boundary condition does not allow each material to operate at its optimal conditions. The efficiency of segmented n-type and p-type legs operating between to heat reservoirs at 400 °C and 200 °C was calculated. With two segments, the total leg efficiency is:

$$\eta_{leg} = \eta_{upper} + (1 - \eta_{upper})\,\eta_{lower} \tag{3.31}$$

In this analysis both the midplane (material transition) temperature in each leg and the current were optimized to maximize the system efficiency. The midplane temperature was adjusted by changing the relative lengths of the thermoelectric materials: lengthening the skutterudite segment decreased the midplane temperature; lengthening the Bi_2Te_3 segment increased the midplane temperature. It was found that the optimal midplane temperature for the n-type leg is 209 °C, even though the n-type ZT curves cross at 212 °C. The optimal midplane temperature for the p-type

leg is 205 °C; the p-type ZT curves cross at 228 °C. It is to be expected that the optimal midplane temperature is not exactly where the ZT curves cross: the efficiency of an element over a ΔT is not just a function of ZT, but also a function of the relative current density at that temperature drop. The performance characteristics of an n-type and p-type leg (optimized independently) are shown in table 3.1. From figure 3-8, it is clear that when the system is optimized for leg efficiency, the individual segments of the legs are not running at peak efficiency due to a small incompatibility of the segments.

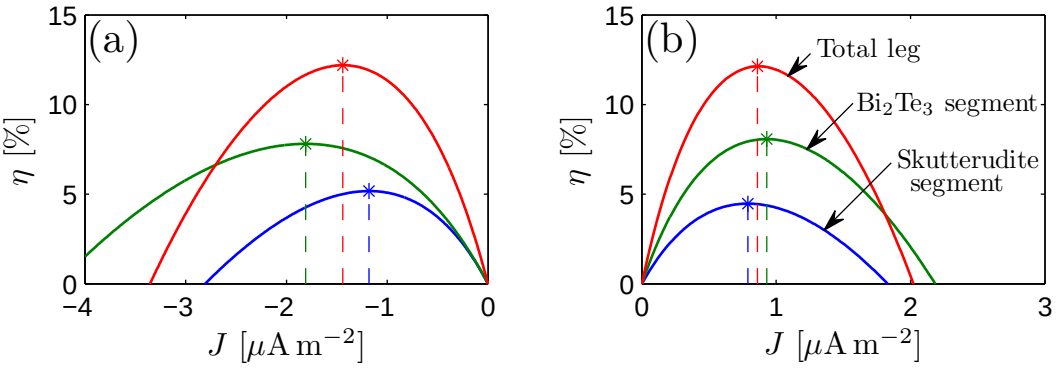

Figure 3-8: Performance of (a) n-type and (b) p-type segmented legs. At optimum leg efficiency (red), the Bi_2Te_3 (green) and skutterudite (blue) segments do not operate at their maxima.

Table 3.1: Individually optimized p- and n-type segmented thermoelectric legs.

	p-type	n-type
T_h [°C]	400	
T_{mid} [°C]	205	209
T_c [°C]	20	
Skutterudite efficiency	4.5%	5.2%
Bi_2Te_3 efficiency	8.0%	7.8%
Leg efficiency	12.1%	12.2%
TEG efficiency	12.2%	

3.5.2 Cascaded Thermoelectrics

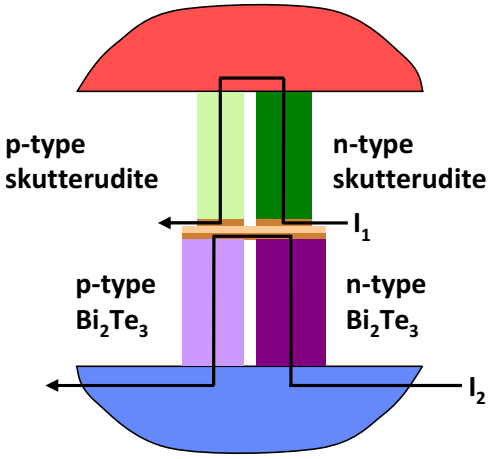

Figure 3-9: A cascaded thermoelectric generator.

Cascaded thermoelectrics are two independent thermoelectric stages joined together. Each stage has its own electrical circuit, which allows the Φ profile to be optimized in each stage for maximum efficiency. Ideally the midplane between the two stages is as thin as possible to reduce the temperature drop from the cold side of the hot stage to the hot side of the cold stage. In addition, the contact resistance to the legs must be small, as each stage in a cascaded thermoelectric adds its own electrical and thermal contact resistances to the device. The thermoelectric stages are modeled as before, and the midplane separating the two stages is modeled as a perfect thermal conductor and a perfect electrical insulator. Figure 3-9 shows the model of a cascaded thermoelectric; table 3.2 describes an optimized Bi_2Te_3/skutterudite cascaded thermoelectric generator operating between two heat reservoirs at 400 °C and 20 °C. This calculation gives the upper limit of performance; details of more exact modeling are presented in the section on advanced modeling.

The performance of cascaded thermoelectrics, single-material thermoelectrics, and segmented thermoelectrics are compared in figure 3-10. In this example, the leg geometries, midplane temperatures, and current have been optimized for mamimum TEG efficiency at a given hot-side temperature with a cold-side temperature of 20 °C. At temperatures below approximately 250 °C, it is not worth stacking skutterudites

Table 3.2: Performance of a cascaded thermoelectric generator.

T_h [°C]	400
T_{mid} [°C]	193
T_c [°C]	20
Skutterudite efficiency	5.2%
Bi_2Te_3 efficiency	7.6%
TEG efficiency	12.4%

on top of Bi_2Te_3 because the skutterudites are less efficient than Bi_2Te_3 in that temperature range. Segmented thermoelectrics can outperform cascaded thermoelectrics if the optimal midplane temperatures for the two legs are very different. This is not the case in this Bi_2Te_3/skutterudite system. At higher temperatures, the performance of the Bi_2Te_3/skutterudite cascaded generator is almost exactly a constant offset above the skutterudite generator. This is due to the fact that the midplane temperature does not increase with increasing hot-side temperature, so at all hot-side temperatures the upper-stage skutterudite is just boosted by the constant power of the Bi_2Te_3 stage. The offset is not exactly constant because the optimal current and thermoelectric potential at the midplane change due to the fact that skutterudites are not completely self-compatible over a large temperature range.

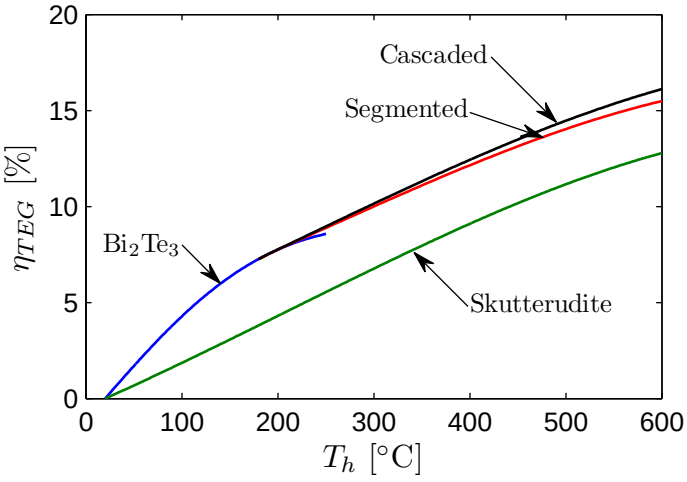

Figure 3-10: Efficiency of Bi_2Te_3, skutterudite, segmented, and cascaded TEGs. The cold side is at 20 °C.

3.6 Solar Thermoelectric Generators

Thermoelectrics can be used for solar energy conversion. A schematic of a solar thermoelectric generator (STEG) is shown in figure 3-11. The collector and thermoelectrics are enclosed in a vacuum in order to effectively eliminate non-radiative thermal losses. The important difference between a STEG and a TEG operating between two heat reserviors is that for a STEG the hot side is not at a fixed temperature: the less heat that is extracted through the thermoelectric legs, the higher the hot-side temperature will be. The efficiency of a STEG, η_{STEG}, is defined as the output electrical power divided by the gross intercepted solar flux. This efficiency can be broken into three components: the optical efficiency, which is the ratio of the power incident on the collector to the gross intercepted power; the collector efficiency, which is the ratio of the heat delivered to the legs to the power incident on the collector; and the TEG efficiency, which is the ratio of the electrical power to the heat delivered to the legs:

$$\eta_{STEG} = \frac{P_{el}}{H_{sol}A_{ap}} = \left(\frac{H_{coll}A_{coll}}{H_{sol}A_{ap}}\right)\left(\frac{Q_h}{H_{coll}A_{coll}}\right)\left(\frac{P_{el}}{Q_h}\right) = \eta_{opt}\eta_{coll}\eta_{TEG} \tag{3.32}$$

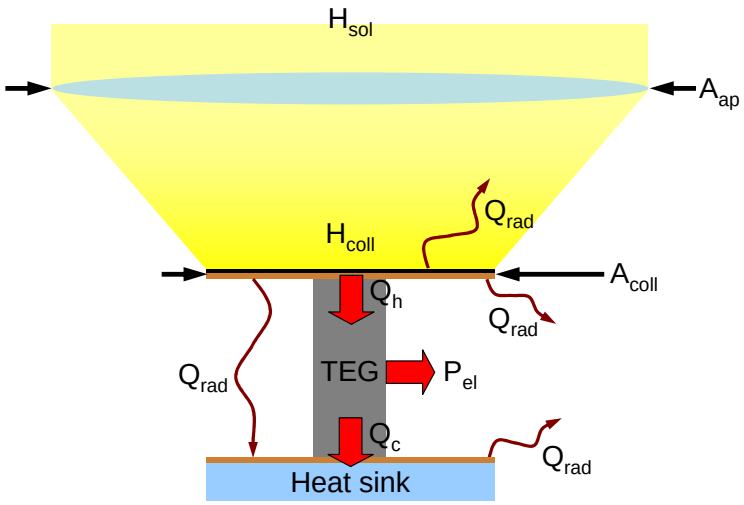

Figure 3-11: Schematic of a concentrating single-generator STEG.

In order to present more general results, the performance can be calculated without the optical efficiency. This efficiency is called the cell efficiency, η_{cell}:

$$\eta_{cell} = \eta_{coll}\eta_{TEG} \tag{3.33}$$

If the optical efficiency is 1, the cell efficiency equals the STEG efficiency. In evacuated systems, the optical efficiency will be at most the transmittance of the glass, which is normally 94%. For concentrating systems, mirror losses will reduce the optical efficiency even further. The efficiency of the collector is calculated from an energy balance on the collector. The TEG efficiency, calculated earlier in this chapter (Fig. 3-10), is then incorporated to calculate the overall STEG efficiency.

3.6.1 Collector Efficiency

The collector efficiency, η_{coll}, is the fraction of intercepted solar flux that is transmitted into the thermoelectric legs. The selective surface absorptance and emittance as well as the surface temperature and ambient temperature determine the heat exchange on the sun-facing surface; the heat losses from the back side of the collector are determined by the system geometry, the emittances and temperatures of the cold sink and the back side of the collector, and the ambient temperature. The back-

side losses can be determined by solving a three-body radiation exchange problem between the collector (body 1), the cold sink (body 2), and the environment (body 3). The radiation network is shown in figure 3-12. A single-subscripted resistance is the surface resistance, and a double-subscripted resistance is a view factor resistance, where F_{ij} is the view factor from surface i to surface j.

$$R_i = \frac{1 - \epsilon_i}{\epsilon_i A_i} \tag{3.34}$$

$$R_{ij} = \frac{1}{A_i F_{ij}} \tag{3.35}$$

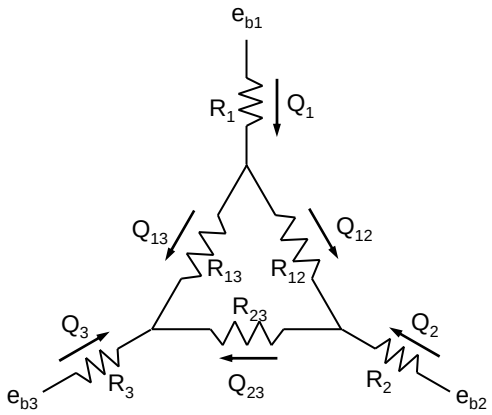

Figure 3-12: Radiation network for STEG heat loss from the back side of the collector.

Writing this network in matrix form with resistors allows the problem to be solved more simply:

$$\begin{bmatrix} R_{12} + R_1 + R_2 & R_1 & -R_2 \\ R_1 & R_{13} + R_1 + R_3 & R_3 \\ -R_2 & R_3 & R_{23} + R_2 + R_3 \end{bmatrix} \begin{bmatrix} Q_{12} \\ Q_{13} \\ Q_{23} \end{bmatrix} = \sigma_{sb} \begin{bmatrix} T_1^4 - T_2^4 \\ T_1^4 - T_3^4 \\ T_2^4 - T_3^4 \end{bmatrix} \tag{3.36}$$

If we denote as M the 3x3 matrix on the left side of equation (3.36), the problem simplifies to:

$$Q_1 = Q_{12} + Q_{13} = A_1\epsilon_{12}\sigma_{sb}\left(T_1^4 - T_2^4\right) + A_1\epsilon_{13}\sigma_{sb}\left(T_1^4 - T_3^4\right) \tag{3.37}$$

$$\epsilon_{12} = \frac{R_{13}R_{23} + R_3\left(R_{12} + R_{13} + R_{23}\right)}{A_1 \det M} \tag{3.38}$$

$$\epsilon_{13} = \frac{R_{12}R_{23} + R_2\left(R_{12} + R_{13} + R_{23}\right)}{A_1 \det M} \tag{3.39}$$

Here Q_1 is the total heat leaving body 1, and ϵ_{12} and ϵ_{13} are the effective emittances from 1 to 2 and 1 to 3, respectively. The heat losses from the back side of the collector are then included in the collector efficiency:

$$\eta_{coll} = \frac{H_{coll}\alpha - \epsilon_{ss}\sigma_{sb}\left(T_h^4 - T_{sky}^4\right) - \epsilon_{12}\sigma_{sb}\left(T_1^4 - T_2^4\right) + \epsilon_{13}\sigma_{sb}\left(T_1^4 - T_2^4\right)}{H_{coll}} \tag{3.40}$$

For this study, a TiNOX selective surface was used. Its absorptance is 0.944 across a broad temperature range, and its temperature-dependent emittance is shown in figure 3-13.

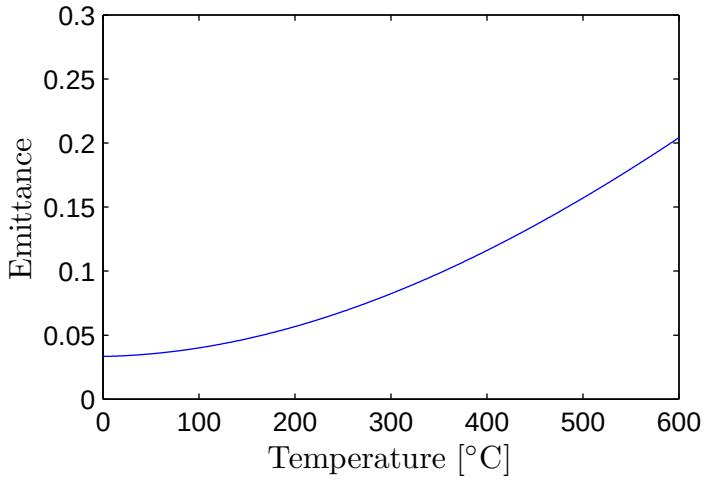

Figure 3-13: Emittance of TiNOX selective surface.

3.6.2 STEG Optimization

We now assume there is an optical system which produces a given incident heat flux onto a collector, and we assume a TEG of known material properties. Both the collector efficiency and the TEG efficiency are functions of the collector (hot-side) and cold-side temperatures. If a fixed cold-side temperature is assumed, we can find the hot-side temperature that maximizes the product of the collector efficiency and the TEG efficiency. Once this optimal hot-side temperature is determined, the geometry and electrical current of the system must be defined so that the temperature, T_h, and heat flow, Q_h, must be equal on both sides of the collector/TEG interface. Previous calculations identified the optimal thermoelectric potential, $\Phi^o_{h,TEG}$, optimal scaled current density, $\widetilde{I}^o$ and optimal ratio of cross-sectional areas, $R^o_{n/p}$ for maximum efficiency at the prescribed hot-side temperature. From these parameters we can determine the configuration of the optimal system. First we recognize that the thermoelectric potential is the ratio of the total heat current to the total electrical current. The total heat current is known from the boundary condition, so we can solve for the optimal current I^o:

$$I^o = \Phi^o_{h,TEG} Q_{h,TEG} = \Phi^o_{h,TEG} \eta_{coll} G_{coll} A_{coll} \tag{3.41}$$

We can substitute this result into the equation for the scaled current density:

$$\widetilde{I}^o = I^o \frac{L}{A_{TEG}} = \Phi^o_{h,TEG} \eta_{coll} G_{coll} \frac{A_{coll}}{A_{TEG}} L \tag{3.42}$$

We define the thermal concentration as the ratio of collector area to thermoelectric leg area: $C_{th} = A_{coll}/A_{TEG}$. The only geometry-related term in equation (3.42) is what we call the geometric parameter, $C_{th}L$. Equations (3.41) and (3.42) lead to the important conclusion that the performance of a STEG with a given incident flux and collector is maximized by controlling the geometric parameter and the current. It is important to note that in order for this to be true, we have to assume that the efficiency of the collector is independent of size, and that there are no other losses like radiation or convection from the legs. The collector efficiency becomes size-dependent

when a temperature gradient is developed across the collector or if the backside view factors change significantly with collector size.

3.7 Multi-stage STEGs

When optical concentration is used for solar thermoelectric generators, the collector can reach temperatures at which it becomes beneficial to use multiple thermoelectric materials. As has been shown before, cascaded STEGs are the most efficient way to convert this heat to electricity. In addition, cascaded STEGs allow some of the heat lost through radiation in the upper stage to be recaptured at the midplane and converted to electricity in the lower stage (Fig. 3-14).

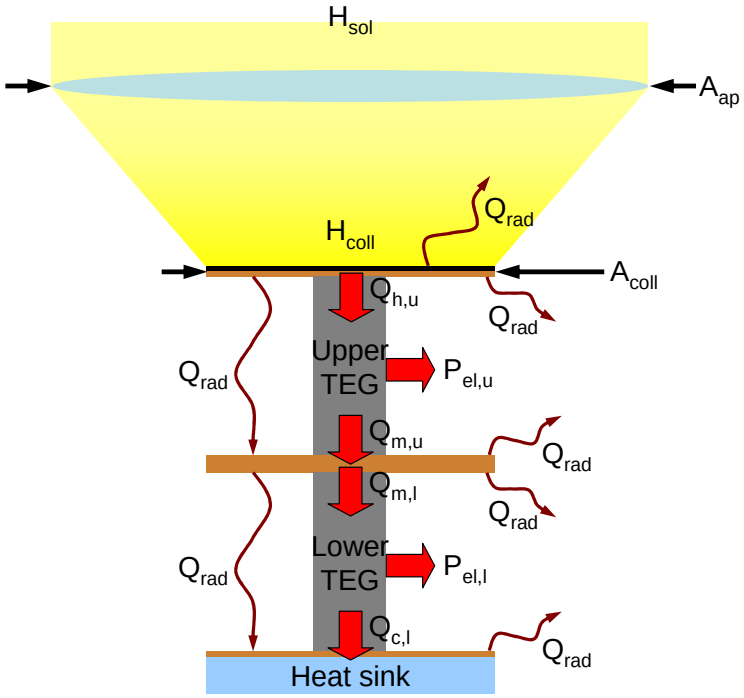

Figure 3-14: Schematic of a concentrating cascaded STEG.

The performance of a cascaded STEG is computed by sweeping through the possible combinations of midplane and hot-side temperatures and finding the maximum efficiency. The lower stage can be optimized as before, by choosing $\Phi_{h,lower}$ and $\widetilde{I}_{lower}$ to optimize the efficiency. The upper stage cannot be optimized as a single-stage STEG with an elevated cold-side temperature at T_m. The waste heat from the upper

stage, as well as some of the radiation losses from the back side of the collector, add to the heat input to the lower stage. The full equation for the power from the device is:

$$P_{total} = A_{coll} H_{coll} \eta_{coll} \eta_{TE,u} + \left[A_{coll} H_{coll} \eta_{coll} \left(1 - \eta_{TE,u}\right) + Q_{13} \right] \eta_{TE,l} \tag{3.43}$$

This optimization was performed over a range of collector incident fluxes. Figure 3-15 compares the efficiency of single-stage Bi_2Te_3, single-stage skutterudite, segmented Bi_2Te_3/skutterudite, and cascaded Bi_2Te_3/skutterudite solar thermoelectric generators as a function of collector incident flux. The hot-side temperatures and midplane temperatures (dashed, where applicable) are shown in figure 3-16. Figure 3-17 shows the corresponding optimal thermal concentration for each system. This assumes that each Bi_2Te_3 leg, skutterudite leg, or Bi_2Te_3/skutterudite segmented leg is 1 mm long. At incident fluxes above approximately $100\,\mathrm{kW\,m^{-2}}$, the thermal concentration drops to low levels such that the area of the back side of the collector is significantly different from the area of the front side of the collector. This does not invalidate the modeling results because this difference has only a small effect on the overall system efficiency. It actually increases the system efficiency slightly by improving the collector efficiency. However for cascaded systems, the optical efficiency at $100\,\mathrm{kW\,m^{-2}}$ is already above 86%, while the maximum is 94.4% due to the absorbtance of the selective surface. The radiation losses from the back side of the collector are less than 30% of the total radiation losses, so changing the back side effective radiating area by 20% would only reduce the radiative losses by 6%. This change would increase the collector efficiency by 0.5%, a negligible amount. Thus the results presented here are still valid for low thermal concentration corresponding to high optical concentration.

At low collector incident fluxes, the best design is the Bi_2Te_3 STEG because the temperature remains low due to the relatively large radiation losses of the collector. For collector incident fluxes above $2\,\mathrm{kW\,m^{-2}}$, multi-material STEGs outperform

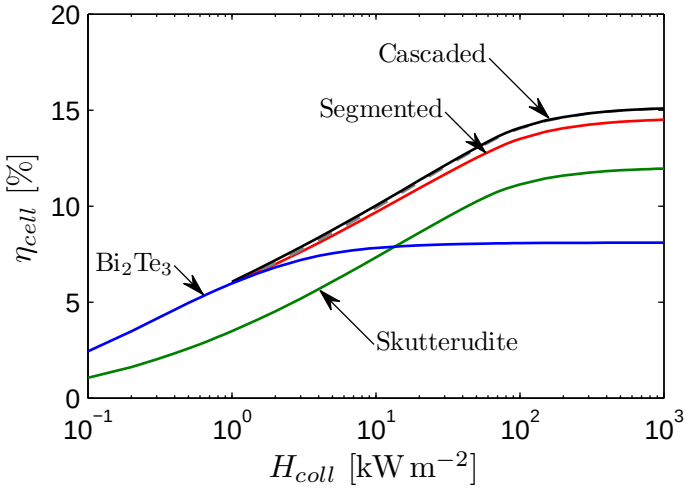

Figure 3-15: Cell efficiency of Bi_2Te_3, skutterudite, segmented, and cascaded thermoelectric STEG cells. The cold side is at 20 °C. The case of the cascade without a midplane is shown in dashed gray.

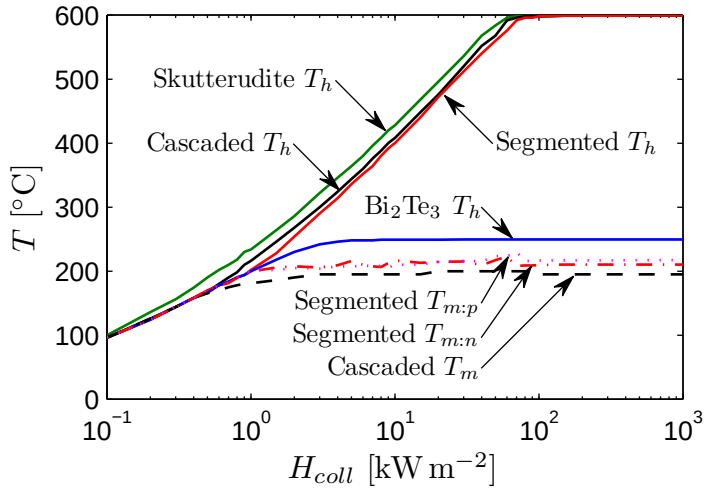

Figure 3-16: Hot-side temperatures T_h of Bi_2Te_3, skutterudite, segmented, and cascaded STEG cells. The cold side is at 20 °C. Also shown are the corresponding midplane temperatures T_m for the cascaded design, and the p-type and n-type midplane temperatures for the segmented STEG cell.

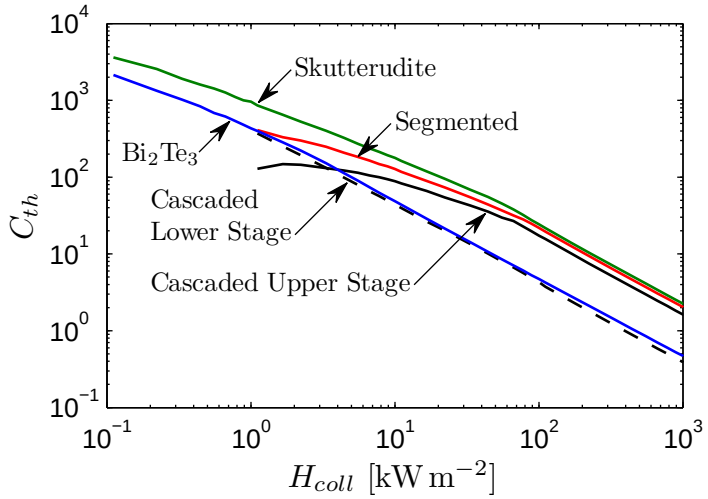

Figure 3-17: Thermal concentration C_{th} for Bi_2Te_3, skutterudite, segmented, and cascaded STEG cells. Each leg, either single-material or segmented, is 1 mm long.

single-stage STEGs. As before, the performance gains of the cascaded device as concentration increases come only from the upper stage because the mid-plane temperature ceases increasing (Fig. 3-16), and thus the device performance is merely a constant offset above the performance of the skutterudite-only stage. Again, a cascaded STEG performs better than a STEG with segmented legs. However, the difference is small. Most of the difference at lower fluxes, and all of the difference at higher fluxes, is due to the higher efficiency of the thermoelectric legs when the current and thermoelectric potential in each material can be optimized. The effect of the midplane acting as a radiation shield is small at 2 kW m^{-2} and almost non-existent at 100 kW m^{-2}. This is because the total flux that leaves the backside of the collector without a radiation shield is only 6% of the total intercepted flux at 2 kW m^{-2}, and only 1% of the intercepted solar flux at 100 kW m^{-2}. The performance of a cascaded STEG without the radiation shield at the midplane is plotted in dashed gray in figure 3-15 for completeness. For these materials, a cascaded design is not much better than a segmented design; given that the extra contact resistance and temperature drops at the midplane were ignored for the cascaded design, it is very likely that a segmented STEG could outperform a cascaded STEG if Bi_2Te_3 and skutterudites are used for the thermoelectric materials.

3.8 STEG Efficiency

The preceding figures predict cell efficiency, which does not include the optical concentration system losses. Figure 3-18 predicts the STEG efficiency for a Bi_2Te_3 STEG and a cascaded STEG with different optical efficiencies. In these cases it is assumed that the solar flux is AM1.5 Direct + Circumsolar ($H_{sol} = 900.1\,\mathrm{W\,m^{-2}}$). A reasonable optical efficiency for this system is 90%, to account for glass transmittance (near 94%) and mirror reflectance (near 95%).

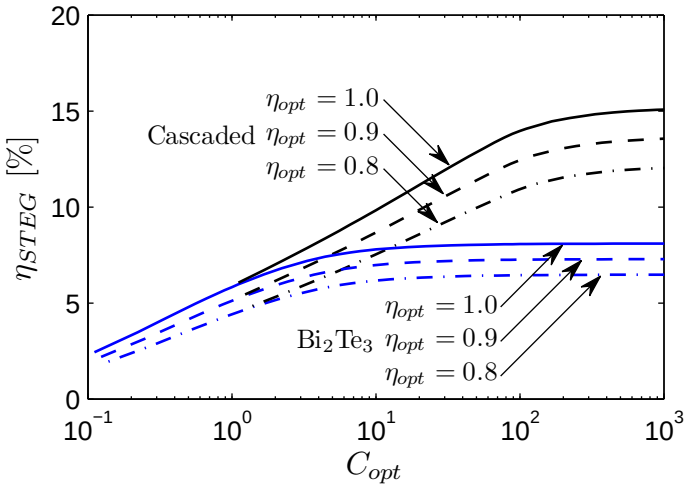

Figure 3-18: STEG efficiency as a function of optical efficiency for STEGs with optical concentration.

3.9 Improvements

From where we currently stand, there are many parameters that could be improved in our system. The two main areas for improvement are the thermoelectric material properties and the selective surface emittance. Figure 3-19 shows the increase in efficiency due to decreasing the thermal conductivity of the thermoelectric materials by 10%, 20%, and 30%. Figure 3-20 shows the increase in efficiency due to decreasing the emittance of the selective surface by 10%, 20%, and 30%. At high incident flux (high optical concentration), the efficiency of the STEGs begins to level off. This is because at high incident flux the collector losses become very small and the

collector efficiency approaches the maximum, which is the absorptance of the collector (94.4% for TiNOX collectors). The efficiency of the TEG levels off at operational temperatures of 600 °C, since this is an enforced upper limit to prevent the material from degrading and melting. In the cases with lower collector emittance, the STEG reaches this ceiling at a lower optical concentration, so the efficiency flattens out faster than in the cases where the emittance is unchanged. The decrease in thermal conductivity has a much larger effect on the system efficiency because it improves the TEG efficiency. The TEG efficiency is far from leveling off at the Carnot limit, so there is still a large gain from decreasing the thermal conductivity.

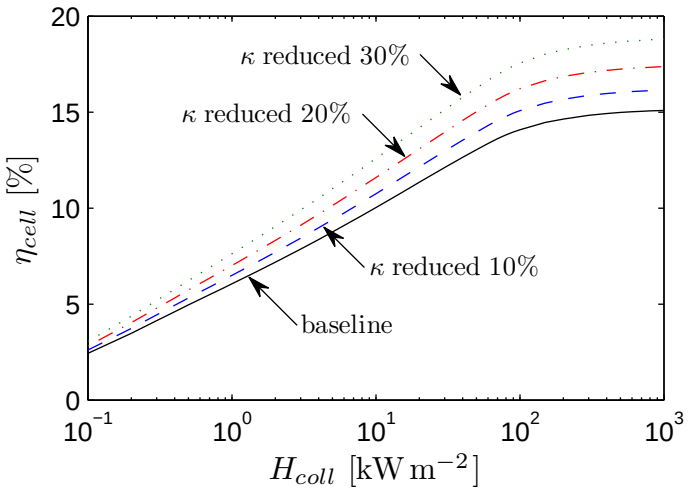

Figure 3-19: Cascaded STEG cell efficiency as a function of flux at the collector. The baseline is compared to a 10%, 20%, and 30% reduction in thermal conductivity.

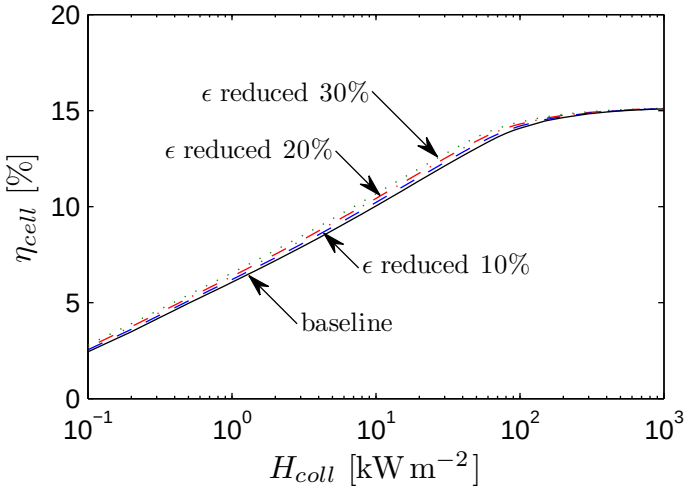

Figure 3-20: Cascaded STEG cell efficiency as a function of flux at the collector. The baseline is compared to a 10%, 20%, and 30% reduction in emittance.

3.10 Summary

In this chapter a method of calculating and optimizing the performance of a thermoelectric leg was presented. From this standard leg model, one can calculate and optimize the performance of thermoelectric generators of various configurations. For TEGs operating over a wide temperature range, it is appropriate to use two different materials systems. Two configurations for wide temperature range applications were compared: segmented legs and cascaded stages. For ideal Bi_2Te_3 and skutterudite systems, the cascaded design achieved slightly higher efficiencies. One can imagine that for other material systems, or for non-ideal cases with large contact resistances or large wire losses, the segmented design could prove to be more efficient than the cascaded design.

Finally, these different TEG designs were incorporated into a solar thermoelectric generator. The conclusions about STEG designs are the same as TEG designs: the cascaded design had a slightly higher efficiency, but small details such as contact resistance, wire losses, mechanical stability, and manufacturability could make the cascaded design the preferred option. Three ways to improve STEG performance are to use concentrating optics, to decrease the emittance of the collector, and to

increase the ZT of thermoelectric materials. Concentration has the largest effect on the efficiency, but increasing the ZT can make a significant difference if the optical concentration is fixed.

Chapter 4

Selective Surfaces for STEGs

The design and optimization of selective surfaces for Carnot applications was described in chapter 2. The optimization of solar thermoelectric generators was presented in chapter 3. In this chapter, the design of selective surfaces specifically for STEG applications is discussed. Limits of performance for STEGs with ideal non-directional selective absorbers are presented.

4.1 Ideal Selective Surfaces for STEGs

In this section, the same analysis technique that was presented in chapter 2 will be applied to STEGs. The optical efficiency is assumed to be 100% in order to present an upper limit on performance. At operating temperatures below 250 °C, a Bi_2Te_3 single-stage STEG will be used; above 250 °C, a cascaded STEG will be used. These two designs represent the highest achievable efficiency over their temperature ranges with our current materials. To achieve the maximum collector performance, the radiation losses from the back side of the collector must be negligible. In this case, the long-wavelength emittance can be zero. Including backside radiation losses is the same as having a long-wavelength emittance value, e, that is greater than zero. Figure 4-1 shows the effect of changing this long-wavelength emittance of the absorber. Given that there will be some long-wavelength radiation from the STEG collector, it is safe to assume that for mid-concentration STEG systems, the selective surface

transition wavelength should be near 1750 nm. Figure 4-1(c) shows that supressing the emittance at high concentration ratios does not increase system performance. In addition, increasing the concentration ratio beyond approximately $C_{opt} = 100$ is not effective because the system is temperature-limited by the materials.

Figure 4-2 and figure 4-3 show the effect of changing the short-wavelength absorption, a, and the width of the transition, w. As seen before in chapter 2, these effects are not nearly as strong as changing the emittance. Changes in the short-wavelength absorption change neither the ideal operating temperature nor the ideal transition wavelength. There is a slight effect on the total hemispherical emittance, but the most prominent effect is on the total hemispherical absorptance. Broadening the transition changes both the emittance and the absorptance, and the jumps in the optimal transition wavelength become less distinct.

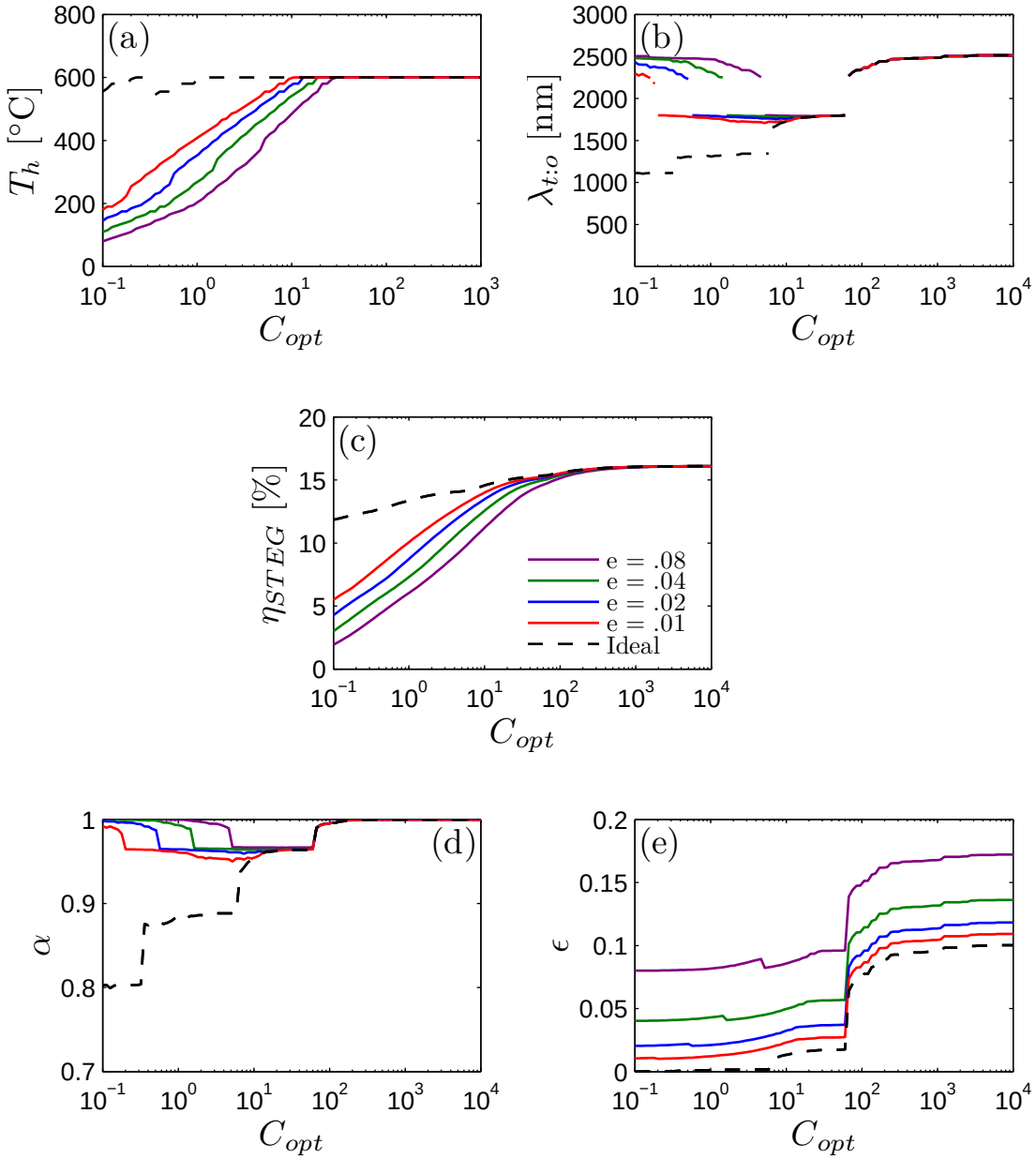

Figure 4-1: Effect of e on STEG optimization: optimum (a) operating temperature, (b) transition wavelength, and (c) STEG efficiency. The resulting total hemispherical (d) absorptance and (e) emittance are shown.

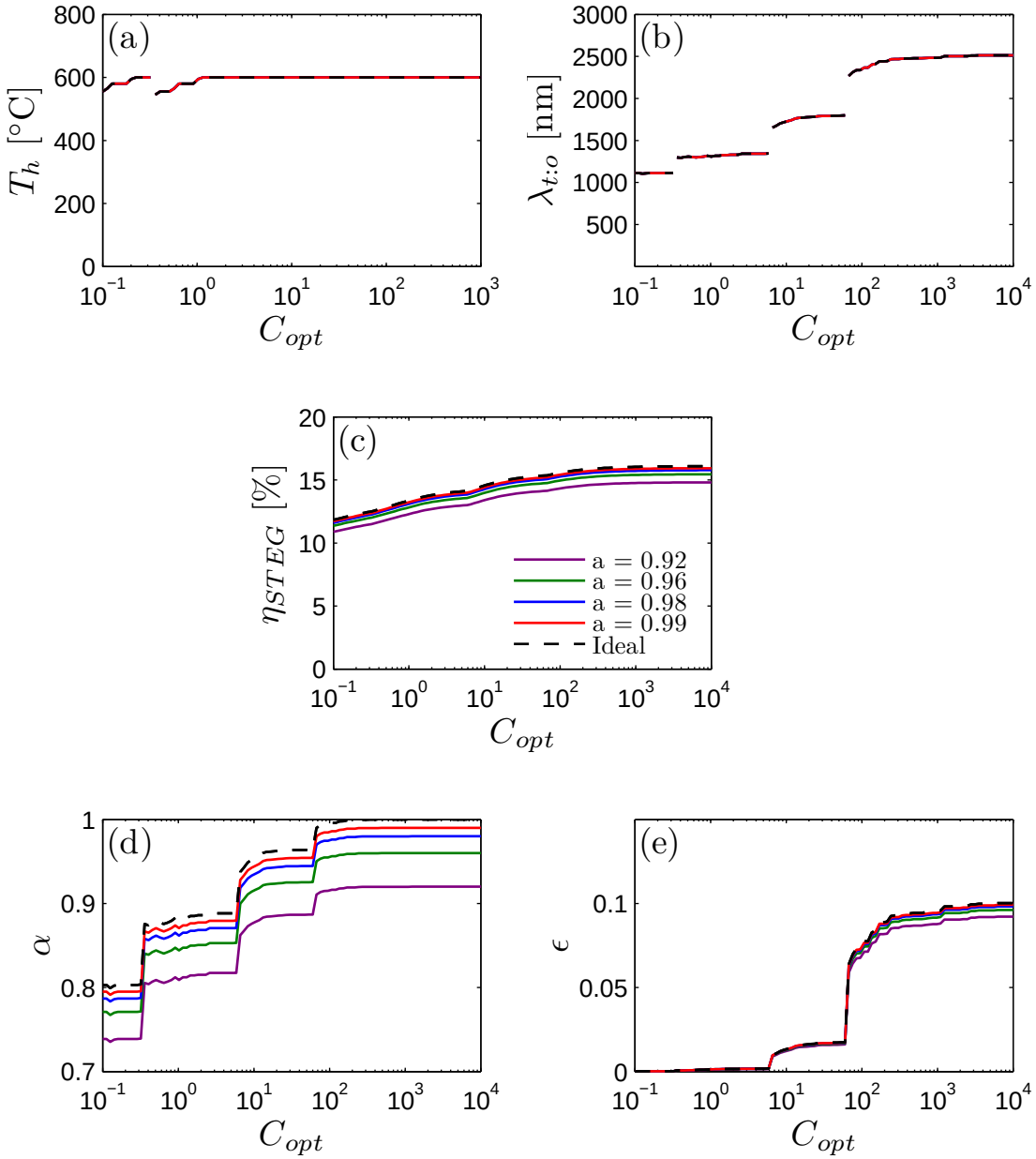

Figure 4-2: Effect of a on STEG optimization: optimum (a) operating temperature, (b) transition wavelength, and (c) STEG efficiency. The resulting total hemispherical (d) absorptance and (e) emittance are shown.

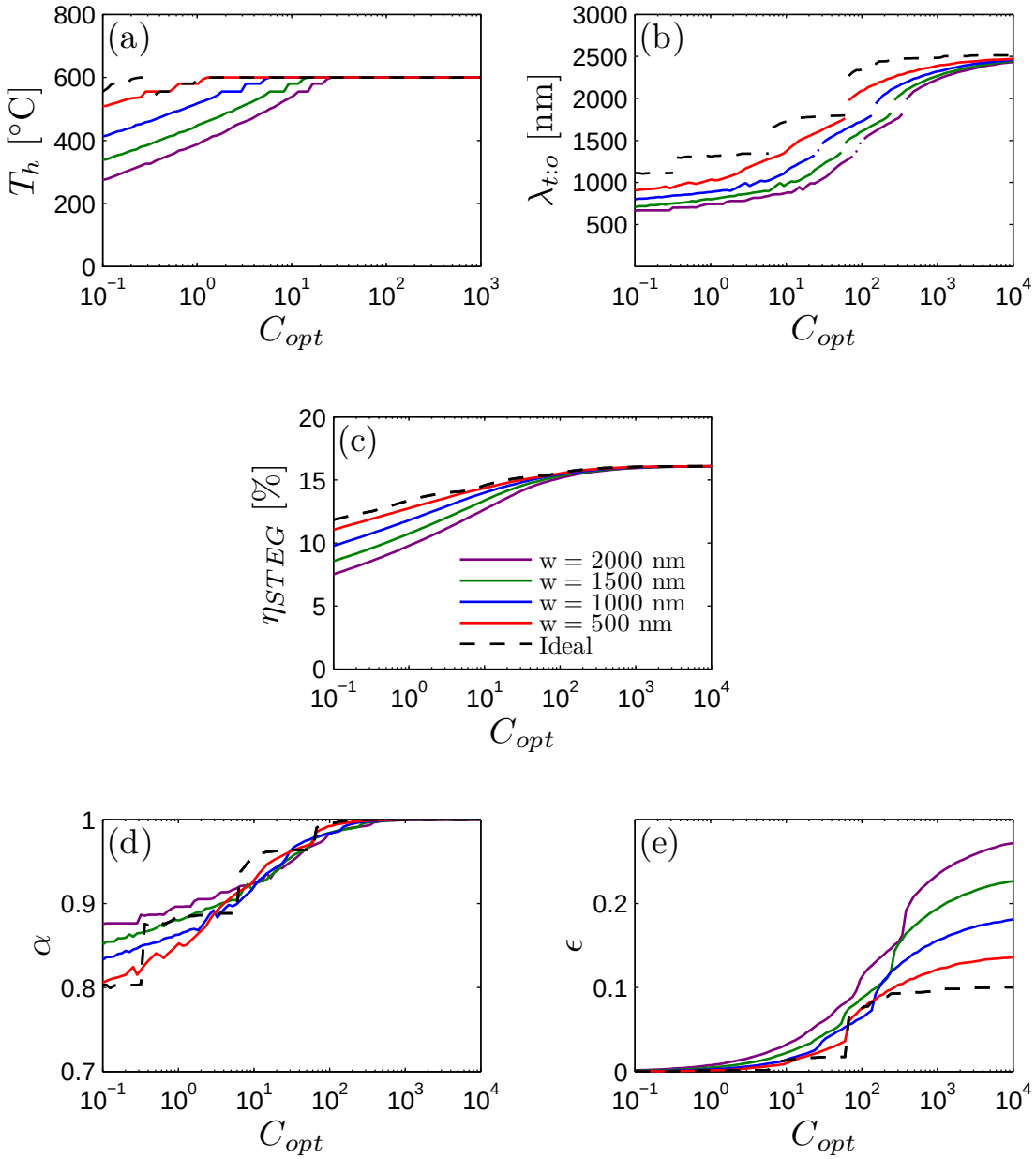

Figure 4-3: Effect of w on system optimization: optimum (a) operating temperature, (b) transition wavelength, and (c) efficiency. The resulting total hemispherical (d) absorptance and (e) emittance are shown.

4.2 Ideal STEG Efficiency Limits

The development of better thermoelectric materials will change the capabilities of STEGs. The Bi_2Te_3 and cascaded designs used in this thesis have an effective $\overline{ZT}$ of near 1 (Fig. 4-4). Using the ideal efficiency equation (Eq. (1.19)), the maximum performance of STEGs with diffuse (non-directional) selective surfaces can be computed. The results are presented in figure 4-5. The $\overline{ZT}$ of the thermoelectric material has very little effect on the ideal properties of a selective absorber for a STEG. Figure 4-5(a) shows that except for very close to two transition regions, the ideal operating temperature is almost solely a function of C_{opt}. Similarly, figure 4-5(b) shows that the ideal transition wavelength is nearly independent of $\overline{ZT}$ also. Not surprisingly, this leads to a nearly-independent absorptance and emittance (Fig. 4-5(d) and Fig. 4-5(e)).

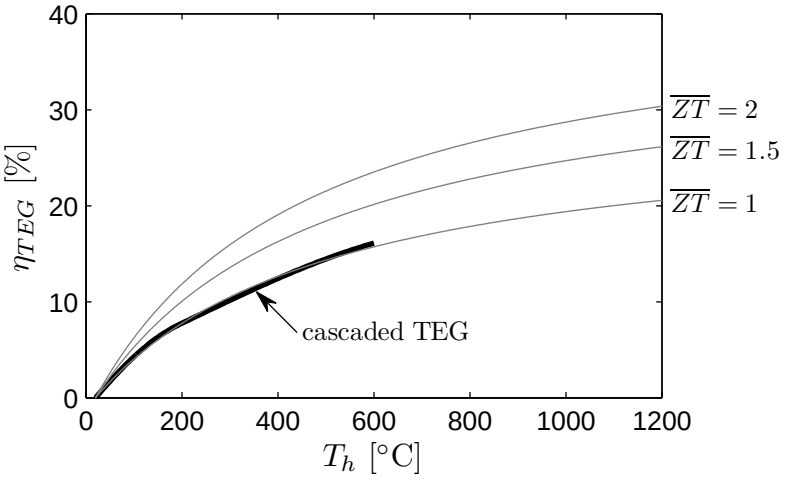

Figure 4-4: STEG efficiency for a cascaded TEG and various ideal TEGs.

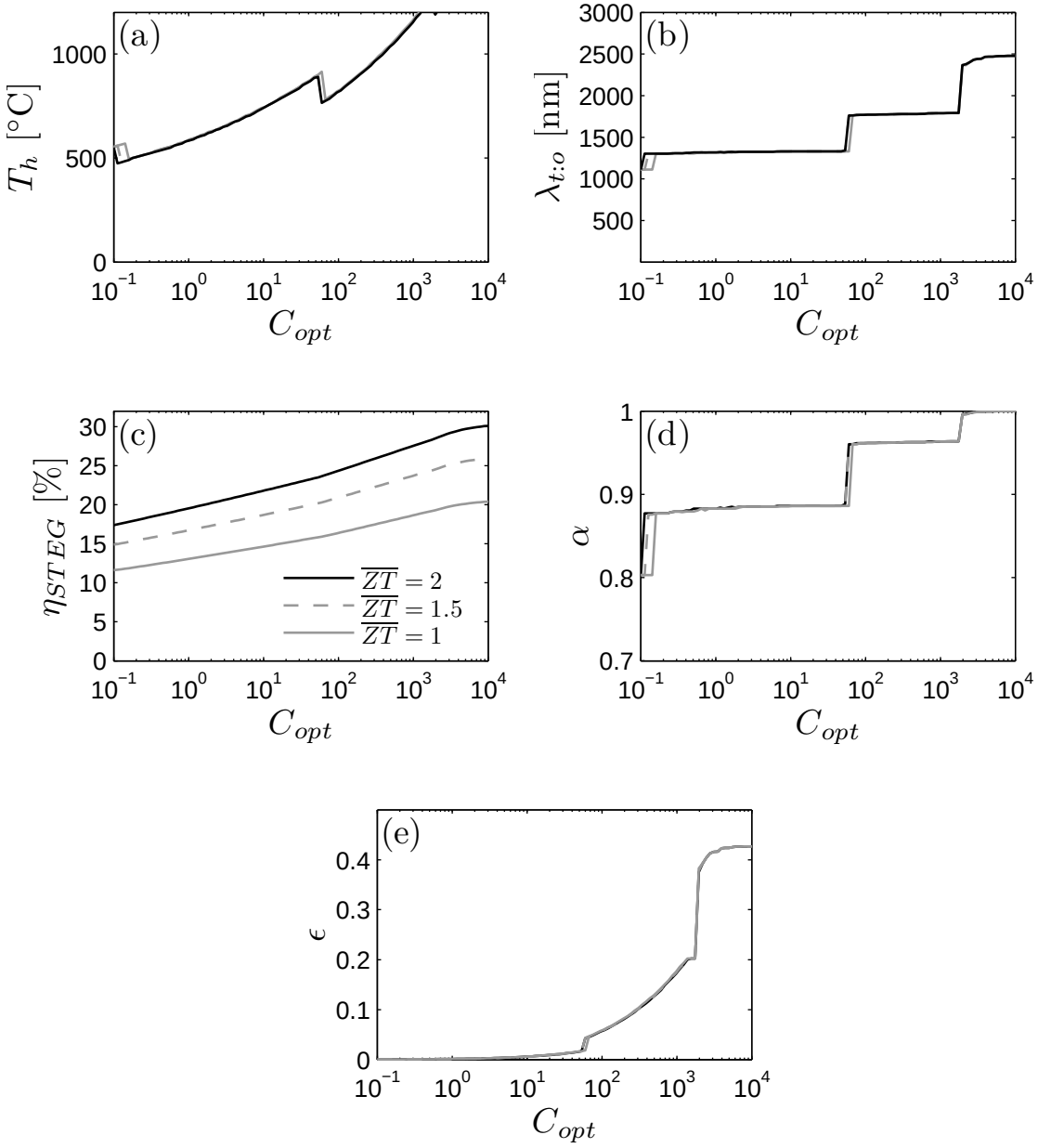

Figure 4-5: Ideal STEG optimization for various $\overline{ZT}$: optimum (a) operating temperature, (b) transition wavelength, and (c) STEG efficiency.

4.3 Conclusion

By developing higher-performing selective surfaces, the efficiency of STEGs can be greatly improved, especially at optical concentration ratios below 10. Unfortunately, the long-wavelength emittance must be completely suppressed to reap the rewards of a better selective surface; reducing it to an epsilon value of even 0.01 still leaves the efficiency far short of the ideal efficiency. While it is very difficult to achieve nearly zero long-wavelength emittance with a traditional selective surface, directional selective surfaces could have great potential for this field (see chapter 5). This analysis also helps target thermoelectric materials development. For all applications with a C_{opt} less than 200, the ideal operating temperature is less than 900 °C, and thus it is not necessary to develop materials that operate above this temperature. Fortunately, materials such as SiGe alloys already are able to operate at these temperatures[30]. We can see that increasing the ZT of a material has a large effect on the performance of a STEG, even if the materials development does not increase the operating temperature of the material. Finally, this analysis presents the upper limit of the performance of STEGs with non-directional absorbers. Depending on the ZT of the materials at hand, the performance limit may help guide whether or not pursuing a solar thermoelectric generator is a reasonable goal.

Chapter 5

Conclusion

5.1 Summary

This thesis investigates two topics related to the harvesting of solar energy: selective surfaces and solar thermoelectric generators. It has been shown that when the absorption bands of the atmosphere are considered, the optimal transition wavelength of an ideal selective surface is nearly universal across applications. There are two key transition wavelengths that together cover nearly all applications: 1750 nm and 2500 nm. In addition, there are fundamental limits of the performance of a selective surface; engineers must be aware of these limits when designing solar thermal devices, as these limits shape the envelope of performance of the device. To design an effective selective surface, the application in which it will be used must be known. At low optical concentrations, the long-wavelength emittance is most important in determining the efficiency of the device. At high optical concentrations, it is the solar absorptance that drives the performance. The specific location of the transition from high emittance to low emittance is important, however the benefits of precisely controlling the position of the transition are usually not nearly as effective as controlling the values of the emittance in the short- or long-wavelength range.

The second topic investigated in this thesis is the design and optimization of a concentrating solar thermoelectric generator. These devices could reach efficiencies above 15% under 100X concentration. It is possible under even low optical concen-

tration ($C_{opt} \approx 2$) to raise the operating temperature of the device to the melting temperature of bismuth telluride compositions. When the temperature exceeds this point, it is beneficial to use a second, high-temperature material such as skutterudites to allow the device to operate at elevated temperatures. The two basic configurations of multi-material thermoelectric generators are cascaded and segmented designs. Cascaded designs have more degrees of freedom, and thus it is possible to achieve a higher theoretical efficiency. Because of the compatibility of skutterudites and Bi_2Te_3, it is possible to design a very effective segmented thermoelectric generator that achieves nearly the same efficiency as a cascaded thermoelectric generator. Given the manufacturing complexity and possible additional losses associated with cascaded designs, a segmented architecture may be easier to build, and may provide better results than a cascaded design.

Solar thermoelectric generators with ideal selective surfaces and perfectly compatible materials (such that the generator efficiency is the ideal ZT efficiency of equation (1.19)) have the potential to reach efficiencies of 20% at high optical concentrations ($C_{opt} = 10,000$) with $\overline{ZT} = 1$ materials, and 30% with a $\overline{ZT}$ of 2. Materials that reach $\overline{ZT} = 2$ can also reach 20% efficiency without optical concentration. In this case, doubling the $\overline{ZT}$ of the material has the same benefit as going from no optical concentration to an optical concentration of 10,000. Without selective surfaces, the efficiency at low optical concentrations is severely affected, as even the best selective surfaces today result in STEG efficiencies of only 5%, compared to 12% with an ideal selective surface. Advances in selective surfaces and thermoelectric materials can both have a large impact in the efficiency of solar thermoelectric generators.

5.2 Future Work

Continuing research into selective surfaces should follow three paths. The first goal is to try to make a selective surface that matches the emittance profile suggested in chapter 2 of this thesis. The ability to create photonic crystals has opened up the possibility of tuning indices of refraction to tailor matter's interactions with light such

that we achieve the desired properties. The second goal would be to take the lessons learned from Tabor's insight and continue to stretch Kirchoff's Law. Tabor exploited the wavelength-dependence of Kirchoff's Law; it would be interesting to find out if we can also exploit the angular dependence of Kirchoff's Law to make an absorber with a strong angular dependence. If so, selective surfaces on tracking systems could become much more effective if they only emitted or absorbed over the small cone of the sky that includes the sun. Finally, it will be critical to be able to test any selective surfaces that we design and build. Therefore it could be very useful to design and build a system to measure the wavelength and angular dependences of emittance at high temperatures.

Before going forward with building a solar thermoelectric generator, it will be important to refine the computer model such that we get a better upper limit on the performance of our devices. A model has already been developed that accounts for electrical and thermal contact resistances and losses through solder and electrodes, but values for these properties must first be measured in order for them to be included in the model. The most important improvement to the model will be including the effect of radiative heat transfer from the thermoelectric legs. At high concentrations, this heat transfer may influence the final STEG architecture. If after these additions the devices still look promising, a cost analysis should be performed to see if a device is worth building. If so, many problems will need to be solved including reducing contact resistance, minimizing or dealing with thermal expansion, creating good adhesion to thermoelectrics, and preventing material degradation over time. The final step would be creating a good design for a heat sink and concentrating optics. When all of these parts are complete, it is possible that solar thermoelectrics will be a viable alternative to solar photovoltaic energy production.

Appendix A

Material Properties

When calculating thermoelectric device performance, the following properties of Bi_2Te_3 materials and skutterudite materials are used (A-1 to A-4). Plotted are the Seebeck coefficient, S, the electrical conductivity, σ, the thermal conductivity, κ, and the dimensionless figure of merit, ZT. These data were graciously provided by our collaborators at Boston College under the guidance of Professor Zhifeng Ren.

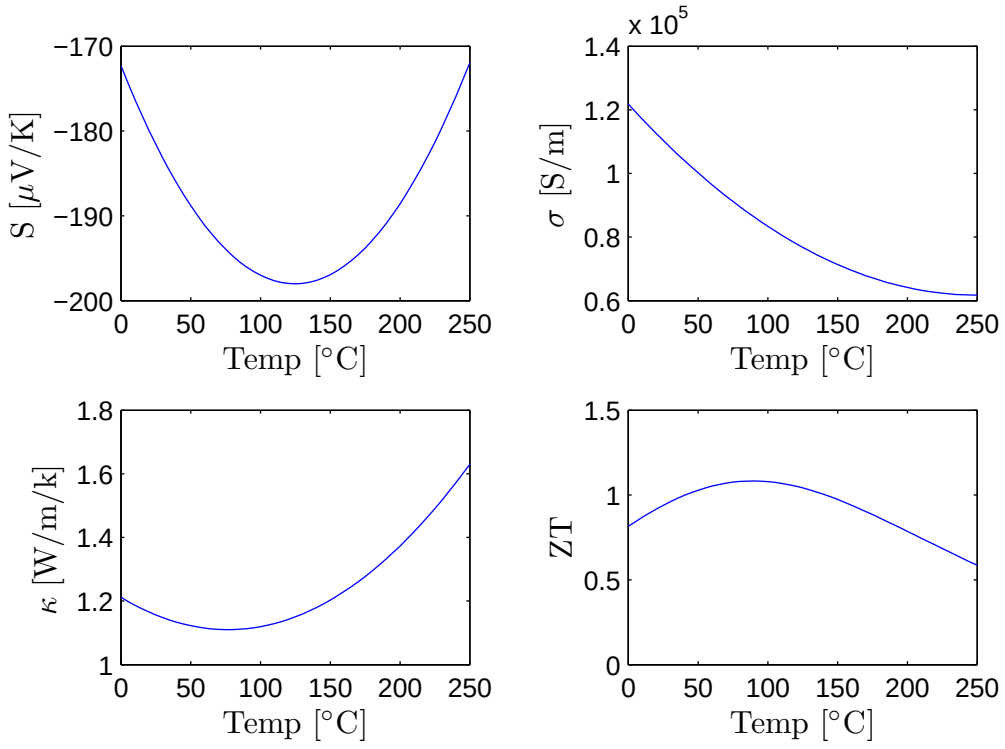

Figure A-1: Thermoelectric properties of the n-type Bi_2Te_3 material used in this thesis.

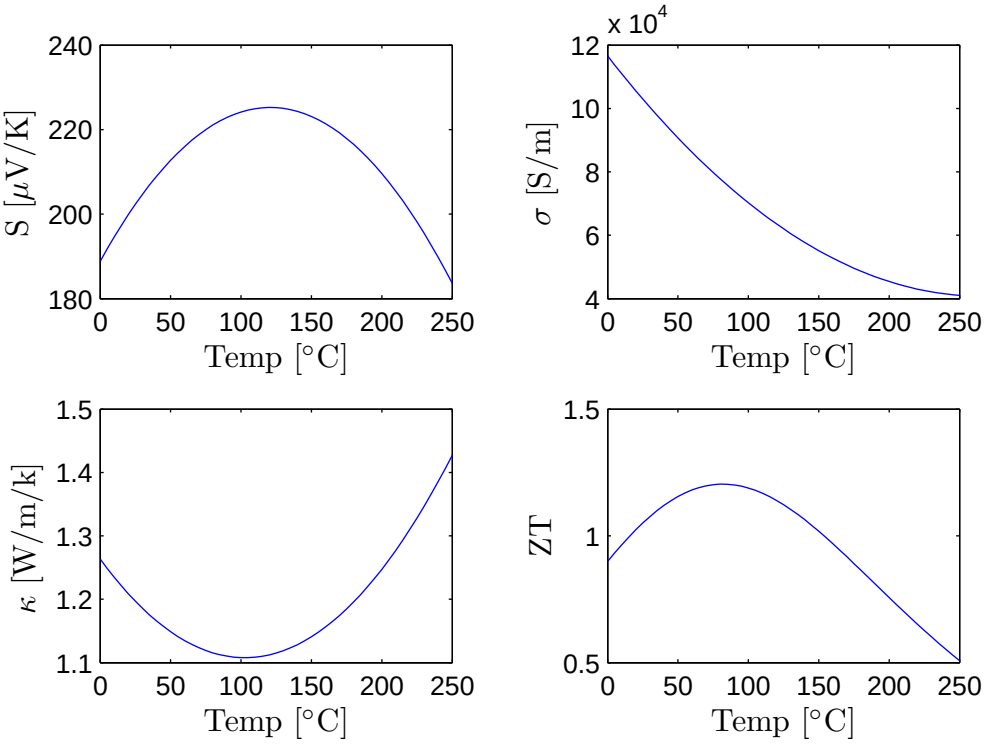

Figure A-2: Thermoelectric properties of the p-type Bi_2Te_3 material used in this thesis.

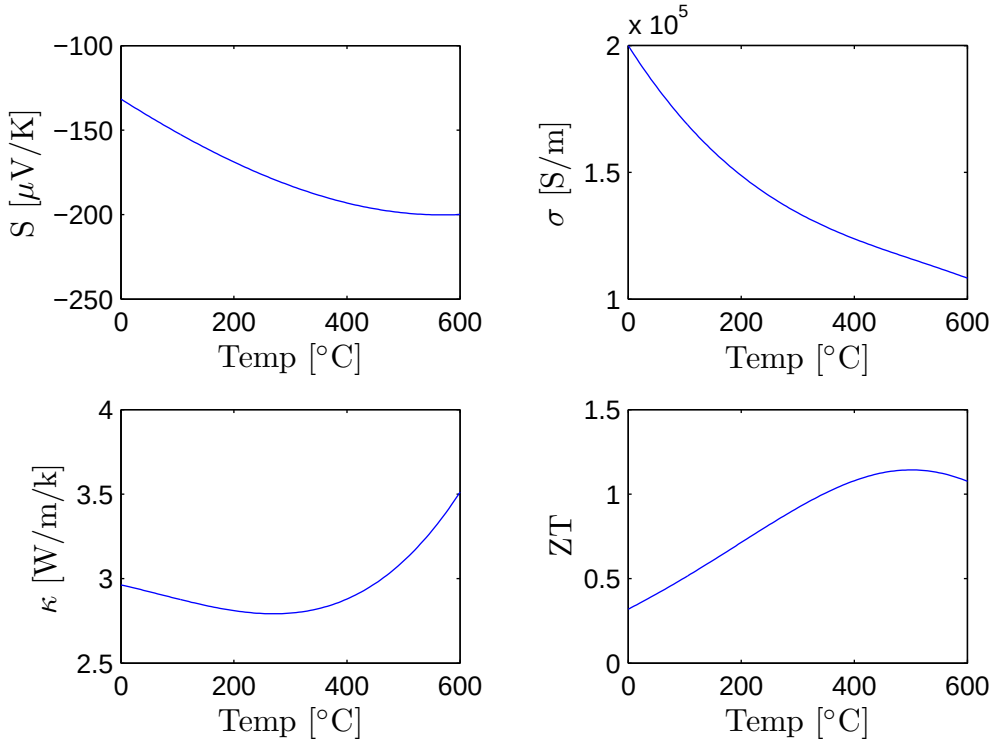

Figure A-3: Thermoelectric properties of the n-type skutterudite used in this thesis.

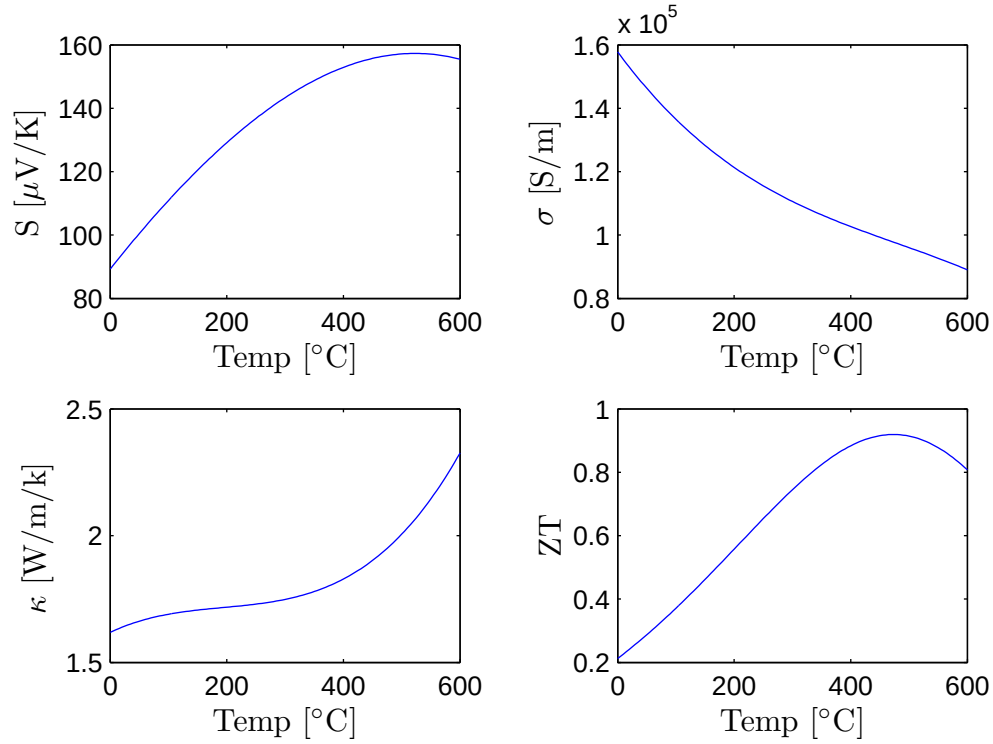

Figure A-4: Thermoelectric properties of the p-type skutterudite used in this thesis.

Bibliography

[1] International energy outlook 2010. Technical Report DOE/EIA-0484(2010), U.S. Energy Information Administration, July 2010.

[2] W. Marion and S. Wilcox. Solar radiation data manual for flat-plate and concentrating collectors. Technical Report NREL/TP-463-5607, National Renewable Energy Laboratory, 1994.

[3] Annual energy outlook 2010. Technical Report DOE/EIA-0383(2010), U.S. Energy Information Administration, April 2010.

[4] Renewables 2010 global status report. Technical report, Renewable Energy Policy Network for the 21st Century, 2010.

[5] M. F. Modest. *Radiative Heat Transfer*. Academic Press, Boston, second edition, 2003.

[6] M. Planck. Über das gesetz der energieverteilung im normalspektrum. *Annalen Der Physik*, 4(3):553–563, March 1901.

[7] R. Winston, J. C. Miñano, and P. Benítez. *Nonimaging Optics*. Academic Press, Boston, 2005.

[8] R. Winston. Solar concentrators. In J. Gordon, editor, *Solar Energy The State of The Art*, chapter 7. James & James Ltd., London, 2001.

[9] W. Szulmayer. A solar strip concentrator. *Solar Energy*, 14(3):327 – 335, 1973.

[10] A. Rabl. Comparison of solar concentrators. *Solar Energy*, 18(2):93 – 111, 1976.

[11] W. Vogel and H. Kalb. *Large-scale Solar Thermal Power*. Wiley, Weinheim, 2010.

[12] D.T. Nelson, D.L. Evans, and R.K. Bansal. Linear fresnel lens concentrators. *Solar Energy*, 17(5):285 – 289, 1975.

[13] R. N. Singh, S. S. Mathur, and T. C. Kandpal. Some geometrical design aspects of a linear fresnel reflector concentrator. *International Journal of Energy Research*, 4:59 – 67.

[14] D. R. Mills. Solar thermal electricity. In J. Gordon, editor, *Solar Energy The State of The Art*, chapter 11. James & James Ltd., London, 2001.

[15] F. Kreith and J. F. Kreider. *Principles of Solar Engineering*. McGraw-Hill, New York, 1978.

[16] H. J. Goldsmid. *Applications of Thermoelectricity*. Methuen and Co., London, 1960.

[17] E. Altenkirch. Über den nutzeffekt der thermosäule. *Physikalische Zeitschrift*, 10(16):560–568, 1909.

[18] E. S. Johansen. Über die vakuumthermosule als strahlungsmesser. *Annalen der Physik*, 338, 1910.

[19] H. J. Goldsmid and R. W. Douglas. The use of semiconductors in thermoelectric refrigeration. *British Journal of Applied Physics*, 5(11):386, 1954.

[20] M. Telkes. The efficiency of thermoelectric generators. I. *Journal of Applied Physics*, 18(12):1116–1127, 1947.

[21] R. W. Fritts. Lead telluride alloys and junctions. In I. B. Cadoff and E. Miller, editors, *Thermoelectric Materials and Devices*, chapter 10. Reinhold Publishing Co., New York, 1960.

[22] V. Fano. Lead telluride and its alloys. In D.M. Rowe, editor, *CRC Handbook of Thermoelectrics*, chapter 21. CRC Press, New York, 1995.

[23] B. Abeles, D. S. Beers, G. D. Cody, and J. P. Dismukes. Thermal conductivity of Ge-Si alloys at high temperatures. *Physical Review*, 125(1):44–46, Jan 1962.

[24] F. D. Rosi. Thermoelectricity and thermoelectric power generation. *Solid-State Electronics*, 11(9):833 – 868, 1968.

[25] L. D. Hicks and M. S. Dresselhaus. Thermoelectric figure of merit of a one-dimensional conductor. *Physical Review B*, 47(24):16631–16634, Jun 1993.

[26] L. D. Hicks and M. S. Dresselhaus. Effect of quantum-well structures on the thermoelectric figure of merit. *Physical Review B*, 47(19):12727–12731, May 1993.

[27] P. F. P. Poudeu, J. D'Angelo, A. D. Downey, J. L. Short, T. P. Hogan, and M. G. Kanatzidis. High thermoelectric figure of merit and nanostructuring in bulk p-type $Na_{1-x}Pb_mSb_yTe_{m+2}$. *Angewandte Chemie International Edition*, 45(23):3835–3839, 2006.

[28] J. Androulakis, C.-H. Lin, H.-J. Kong, C. Uher, C.-I Wu, T. Hogan, B. A. Cook, T. Caillat, K. M. Paraskevopoulos, and M. G. Kanatzidis. Spinodal decomposition and nucleation and growth as a means to bulk nanostructured

thermoelectrics: Enhanced performance in $Pb_{1-x}Sn_xTe - PbS$. *Journal of the American Chemical Society*, 129(31):9780–9788, 2007.

[29] J. P. Heremans, V. Jovovic, E. S. Toberer, A. Saramat, K. Kurosaki, A. Charoenphakdee, S. Yamanaka, and G. J. Snyder. Enhancement of thermoelectric efficiency in PbTe by distortion of the electronic density of states. *Science*, 321(5888):554–557, 2008.

[30] G. J. Snyder and E. S. Toberer. Complex thermoelectric materials. *Nature Materials*, 7(2):105–114, 2008.

[31] A. J. Minnich, M. S. Dresselhaus, Z. F. Ren, and G. Chen. Bulk nanostructured thermoelectric materials: current research and future prospects. *Energy and Environmental Science*, 2:466–479, 2009.

[32] A. S. E. Ackermann. The utilization of solar energy. *Annual Report Smithsonian Institution*, pages 141–166, 1915.

[33] L. Simonin. L'emploi industriel de la chaleur solaire. In *Revue des Deux Mondes*. 1876.

[34] W. Wien. Temperatur und entropie der strahlung. *Annalen der Physik*, 288(5):132–165, 1894.

[35] H. Tabor. Selective radiation. I: wavelength discrimination. *Bulletin of the Research Council of Israel*, 5A(2):119–128, 1956.

[36] L. Harris, R. T. McGinnies, and B. M. Siegel. The preparation and optical properties of gold blacks. *Journal of the Optical Society of America*, 38(7):582–588, 1948.

[37] A. H. Pfund. The optical properties of metallic and crystalline powders. *Journal of the Optical Society of America*, 23(10):375–377, 1933.

[38] H. Tabor. Selective radiation. II: wavefront discrimination. *Bulletin of the Research Council of Israel*, 5A(2):129–134, 1956.

[39] L. H. Shaffer. Wavelength-dependent (selective) processes for the utilization of solar energy. *Solar Energy*, 2(3-4):21 – 26, 1958.

[40] R. B. Gillette. Selectively emissive materials for solar heat absorbers. *Solar Energy*, 4(4):24 – 32, 1960.

[41] D. K. Edwards, J. T. Gier, K. E. Nelson, and R. D. Roddick. Spectral and directional thermal radiation characteristics of selective sufaces for solar collectors. *Solar Energy*, 6(1):1 – 8, 1962.

[42] C. H. Liebert and R. R. Hibbard. Performance of spectrally selective collector surfaces in a solar-driven carnot space-power system. *Solar Energy*, 6(3):84 – 88, 1962.

[43] R. A. Cross. From other literature properties required for collector surfaces of solar-powered thermal systems. *Solar Energy*, 7(3):152 – 155, 1963.

[44] R. N. Schmidt. Effectiveness of solar absorber surfaces. *Journal of Spacecraft and Rockets*, 2(1):101 – 102, 1965.

[45] J. Jurisson, R. E. Peterson, and H. Y. B. Mar. Principles and applications of selective solar coatings. *Journal of Vacuum Science and Technology*, 12(5):1010–1015, 1975.

[46] J. Spitz. Selective surfaces for high temperature solar photothermal conversion. *Thin Solid Films*, 45(1):31 – 41, 1977.

[47] R. Pasquetti and F. Papini. Thermal conversion of solar radiation theoretical performance of collectors furnished with an absorbent selective surface. *Solar Energy*, 21(2):129 – 138, 1978.

[48] B. O. Seraphin. *Spectrally Selective Surfaces and Their Impact on Photothermal Solar Energy Conversion*, chapter 2, pages 5–55. Springer-Verlag, New York, 1979.

[49] D. R. Mills. Limits of solar selective surface performance. *Applied Optics*, 24(20):3374–3380, 1985.

[50] P. Moon. Proposed standard solar-radiation curves for engineering use. *Journal of the Franklin Institute*, 230(5):583 – 617, 1940.

[51] R. E. Bird, R. L. Hulstrom, and L. J. Lewis. Terrestrial solar spectral data sets. *Solar Energy*, 30(6):563 – 573, 1983.

[52] Reference solar spectral irradiances: Direct normal and hemispherical on 37° tilted surface. Technical Report ASTM Standard G 173-03, ASTM International, 2008.

[53] Solar constant and zero air mass solar spectral irradiance tables. Technical Report ASTM Standard E 490-00a, ASTM International, 2006.

[54] C. E. Kennedy. Review of mid- to high-temperature solar selective absorber materials. Technical Report TP-520-31267, National Renewable Energy Laboratory, July 2002.

[55] D. M. Trotter Jr. and A. J. Sievers. Thermal emissivity of selective surfaces—new lower limits. *Applied Physics Letters*, 35(5):374–376, 1979.

[56] D. M. Trotter Jr. and A. J. Sievers. Spectral selectivity of high-temperature solar absorbers. *Applied Optics*, 19(5):711–728, 1980.

[57] D. R. Mills and L. C. Botten. Lower emissivity limits indicated for high temperature selective surfaces. *Applied Optics*, 22(20):3182–3190, 1983.

[58] C. G. Granqvist. Solar-energy materials - overview and some examples. *Applied Physics A*, 52(2):83–93, Feb 1991.

[59] E. Randich and R.B. Pettit. Solar selective properties and high temperature stability of CVD ZrB_2. *Solar Energy Materials*, 5(4):425 – 435, 1981.

[60] Qi-Chu Zhang, J. C. Kelly, and D. R. Mills. Possible high absorptance and low emittance selective surface for high temperature solar thermal collectors. *Applied Optics*, 30(13):1653–1658, May 1991.

[61] B.O. Seraphin. Chemical vapor deposition of spectrally selective surfaces for high temperature photothermal conversion. *Thin Solid Films*, 57(2):293 – 297, 1979.

[62] K. C. Park. The extreme values of reflectivity and the conditions for zero reflection from thin dielectric films on metal. *Applied Optics*, 3(7):877–881, Jul 1964.

[63] R. N. Schmidt and K. C. Park. High-temperature space-stable selective solar absorber coatings. *Applied Optics*, 4(8):917–925, Aug 1965.

[64] I. T. Ritchie and B. Window. Applications of thin graded-index films to solar absorbers. *Applied Optics*, 16(5):1438–1443, 1977.

[65] S. Esposito, A. Antonaia, M. L. Addonizio, and S. Aprea. Fabrication and optimisation of highly efficient cermet-based spectrally selective coatings for high operating temperature. *Thin Solid Films*, 517(21):6000 – 6006, 2009.

[66] J. J. Cuomo, J. F. Ziegler, and J. M. Woodall. A new concept for solar energy thermal conversion. *Applied Physics Letters*, 26(10):557–559, 1975.

[67] Z.-C. Jin, I. Hamberg, and C. G. Granqvist. Optical properties of sputter-deposited zno:al thin films. *Journal of Applied Physics*, 64(10):5117–5131, 1988.

[68] E. Weston. U.S. Patent No. 389,124, 1888.

[69] W. W. Coblentz. U.S. Patent No. 1,077,219, 1913.

[70] M. Telkes. Solar thermoelectric generators. *Journal of Applied Physics*, 25(6):765–777, 1954.

[71] R. Rush. Solar flat plate thermoelectric generator research. Technical report, General Instrument Corporation, June 1963.

[72] R. Rush. Solar flat plate thermoelectric generator research. Technical Report APL TDR 64-87, General Instrument Corporation, September 1964.

[73] V. Raag. Solar thermoelectric generator design and panel development program. Technical Report CR-72340, NASA, December 1967.

[74] V. Raag. Flat-plate solar thermoelectric generators for solar probe missions. Technical Report TMX-52451, NASA, 1968.

[75] N. Fuschillo, R. Gibson, F. K. Eggleston, and J. Epstein. Flat plate solar thermoelectric generator for near-earth orbits. *Advanced Energy Conversion*, 6(2):103 – 118, IN3–IN6, 119–125, 1966.

[76] N. Fuschillo and R. Gibson. Germanium-silicon, lead telluride, and bismuth telluride alloy solar thermoelectric generators for venus and mercury probes. *Advanced Energy Conversion*, 7(1):43 – 52, 1967.

[77] H. J. Goldsmid, J. E. Giutronich, and M. M. Kaila. Solar thermoelectric generation using bismuth telluride alloys. *Solar Energy*, 24(5):435 – 440, 1980.

[78] D. M. Rowe. A high performance solar powered thermoelectric generator. *Applied Energy*, 8(4):269 – 273, 1981.

[79] E. A. Movsumov and A. M. Bairamov. Regime characteristics of a solar thermoelectric generator and comparison of experimental and calculated data. *Geliotekhnika*, 16(6):69–70, 1980.

[80] C. L. Dent and M. H. Cobble. A solar thermoelectric generator and analysis. In *Proceedings of the Fourth International Conference on Thermoelectric Energy Conversion*, pages 75–78, Arlington, TX, 1982.

[81] Jr. A. S. Roberts and K. E. Shaheen. Hybrid thermoelectric solar collector design and analysis. *Journal of Solar Energy Engineering*, 104(4):373–377, 1982.

[82] N. S. Lidorenko, O. P. Astakhov, and N. V. Kolomoets. Research on solar thermoelectric cells with a flat plate collector. *Geliotekhnika*, 20(3):7–9, 1984.

[83] H. Scherrer, L. Vikhor, B. Lenoir, A. Dauscher, and P. Poinas. Solar thermolectric generator based on skutterudites. *Journal of Power Sources*, 115(1):141 – 148, 2003.

[84] G. Rockendorf, R. Sillmann, L. Podlowski, and B. Litzenburger. PV-hybrid and thermoelectric collectors. *Solar Energy*, 67(4-6):227 – 237, 1999.

[85] C. A. Mgbemene, J. Duffy, H. Sun, and S. O. Onyegegbu. Electricity generation from a compound parabolic concentrator coupled to a thermoelectric module. *ASME Conference Proceedings*, 2008(43208):423–432, 2008.

[86] R. Amatya and R. Ram. Solar thermoelectric generator for micropower applications. *Journal of Electronic Materials*, 39:1735–1740, 2010. 10.1007/s11664-010-1190-8.

[87] A. Agbossou, Q. Zhang, G. Sebald, and D. Guyomar. Solar micro-energy harvesting based on thermoelectric and latent heat effects. part I: Theoretical analysis. *Sensors and Actuators A*, 163(1):277 – 283, 2010.

[88] Q. Zhang, A. Agbossou, Z. Feng, and M. Cosnier. Solar micro-energy harvesting based on thermoelectric and latent heat effects. part II: Experimental analysis. *Sensors and Actuators A*, 163(1):284 – 290, 2010.

[89] J. Chen. Thermodynamic analysis of a solar-driven thermoelectric generator. *Journal of Applied Physics*, 79(5):2717–2721, 1996.

[90] V. L. Kuznetsov. Functionally graded materials for thermoelectric applications. In D. M. Rowe, editor, *Thermoelectrics Handbook: Macro to Nano*, chapter 38. CRC Press, New York, 2006.

[91] T. P. Hogan and T. Shih. Modeling and characterization of power generation modules based on bulk materials. In D. M. Rowe, editor, *Thermoelectrics Handbook: Macro to Nano*, chapter 12. CRC Press, New York, 2006.

[92] D. Kraemer. Research on the solar application of thermoelectric generators. Master's thesis, Swiss Federal Institute of Technology Zurich, Department of Mechanical Engineering, May 2007.

[93] C. A. Domenicali. Irreversible thermodynamics of thermoelectric effects in inhomogeneous, anisotropic media. *Physical Review*, 92(4):877–881, Nov 1953.

[94] H. B. Callen. The application of onsager's reciprocal relations to thermoelectric, thermomagnetic, and galvanomagnetic effects. *Physical Review*, 73(11):1349–1358, Jun 1948.

[95] S. R. de Groot. *Thermodynamics of Irreversible Processes*. Interscience Publishers, New York, 1951.

[96] L. Onsager. Reciprocal relations in irreversible processes. I. *Physical Review*, 37(4):405–426, Feb 1931.

[97] L. Onsager. Reciprocal relations in irreversible processes. II. *Physical Review*, 38(12):2265–2279, Dec 1931.

[98] G. J. Snyder and T. S. Ursell. Thermoelectric efficiency and compatibility. *Physical Review Letters*, 91(14):148301, Oct 2003.

[99] G. J. Snyder. Thermoelectric power generation: Efficiency and compatibility. In D. M. Rowe, editor, *Thermoelectrics Handbook: Macro to Nano*, chapter 9. CRC Press, New York, 2006.

[100] T. C. Harman. Multiple stage thermoelectric generation of power. *Journal of Applied Physics*, 29(10):1471–1473, 1958.